NOVEL HYBRID PEROVSKITE CATALYSTS

FOR DE-NO_X APPLICATIONS

A THESIS SUBMITTED TO

THE GRADUATE SCHOOL OF ENGINEERING AND SCIENCE

OF BILKENT UNIVERSITY

IN PARTIAL FULFILLMENT OF THE REQUIREMENTS FOR

THE DEGREE OF

MASTER OF SCIENCE

IN

CHEMISTRY

By

Kerem Emre Ercan

September, 2015

NOVEL HYBRID PEROVSKITE CATALYSTS FOR DE-NO_X APPLICATIONS

By Kerem Emre Ercan

September, 2015

We certify that we have read this thesis and that in our opinion it is fully adequate, in scope and in quality, as a thesis for the degree of Master of Science.

_____

Assoc. Prof. Dr. Emrah Özensoy (Advisor)

_____

Assist. Prof. Dr. Bilge Baytekin

_____

Assoc. Prof. Dr. Okan Esentürk

Approved for the Graduate School of Engineering and Science:

_____

Prof. Dr. Levent Onural

Director of the Graduate School

ABSTRACT

NOVEL HYBRID PEROVSKITE CATALYSTS FOR DE-NO_X APPLICATIONS

Kerem Emre Ercan
M.S. in Chemistry
Advisor: Assoc. Prof. Dr. Emrah Özensoy
September, 2015

The main purpose of this study is to identify the nature of hybrid perovskites in the form of $LaCo_xMn_{1-x}O_3$ (x=0.0-1.0) for catalytic De-NO_x applications. Characteristic structure, thermal stability and NO_x/SO_x adsorption/release properties of perovskites were studied by XRD, BET, XPS, in-situ FTIR, ex-situ FTIR, TEM, BET, TPD and TPR. $LaCo_{0.8}Mn_{0.2}$ and $LaCo_{0.7}Mn_{0.3}O_3$ were found to yield the highest NO_x storage Capacity (NSC) among other investigated perovskites due to their optimized B-site composition. NO_x and SO_x adsorption experiments pointed out that B-site substitution did not have a significant alteration on adsorption geometries of corresponding adsorbates. NO_x uptakes of the investigated perovskites were observed to be enhanced via H_2 reduction as verified by IR results. Furthermore, N_2 (28 a.m.u) release monitored by QMS during NO_x TPD revealed direct N-O bond activation and complete reduction of NO_x species under certain conditions. SO_x adsorption and reduction experiments suggested that SO_x reduction via H_2 is more effective for Mn-enrich perovskites, since Co-enriched materials formed irreversible sulfate species. It was observed that adsorbed NO_x species can be readily replaced by SO_x species in the co-presence of NO_x and SO_x. It was also demonstrated that the oxygen-defect density and the surface oxygen concentration of hybrid perovskites

can be modified by fine-tuning the substitution at the B-site. Based on ex-situ FTIR results, it was established that Co-O linkages could be gradually replaced with Mn-O linkages by increasing the Mn loading in the perovskite composition. Furthermore, specific surface areas (SSA) of hybrid perovskites were found to be enhanced by increasing the Mn loading. Current results suggest that hybrid perovskites are promising novel catalytic architectures for De-NO_x applications due to their high NSC and versatile chemical structure which can be fine-tuned to enhance SO_x tolerance, redox properties and thermal stability.

Keywords: Perovskite, NO_x, SO_x, $LaMnO_3$, $LaCoO_3$, $LaCo_xMn_{1-x}O_3$

ÖZET

De-NO_x UYGULAMALARI İÇİN YENİ NESİL HİBRİT PEROVSKİTLER

Kerem Emre Ercan
Kimya, Yüksek Lisans
Tez Danışmanı: Doç. Dr. Emrah Özensoy
Eylül, 2015

Bu çalışmanın temel amacı, katalitik De-NO_x uygulamalarına yönelik, $LaCo_xMn_{1-x}O_3$ tipi hibrit perovskit malzemelerinin, yapısal ve işlevsel özelliklerinin incelenmesidir. Perovskitlerin karakteristik yapısı, termal dayanıklılıkları ve NO_x/SO_x adsrobsiyon/salınım özellikleri XRD, BET, XPS, in-situ FTIR, ex-situ FTIR, TEM, BET, TPD ve TPR teknikleri kullanılarak çalışılmıştır. Diğerlerine kıyasla, $LaCo_{0.8}Mn_{0.2}$ve$LaCo_{0.7}Mn_{0.3}O_3$ perovskitlerinin optimize edilmiş yüzeyleri sayesinde (yani özel B-noktası kompozisyonu nedeniyle),en yüksek NO_x depolama kapasitesine sahip malzemeler oldukları belirlenmiştir. NO_x ve SO_x deneyleri, B noktalarına ait kompozisyonun, katalizör yüzeyine bağlanan türlerin adsorpsiyon geometrisi üzerinde önemli bir değişikliğe yol açmadığını göstermiştir. Diğer taraftan, NO_x emiliminin H_2 indirgenmesi sonrasında arttığı, IR deneyleriyle gösterilmiştir. Ayrıca, QMS deneylerinde ölçülen N_2, özel koşullar altında, hibrit katalizörlerin N-O bağ aktivasyonunu başarıyla gerçekleştirebildiğini ve NO_x türlerinin tamamen indirgenebildiğini göstermektedir. Mn'ce zengin perovskitler üzerindeki SO_x türleri, H_2 ile oldukça etkin bir şekilde indirgenerek, bertaraf edilebilmesine rağmen; Co'ca zengin perovskitlerde tersinmez sülfat türleri oluşumu

nedeniyle kükürt giderim sürecinin daha verimsiz olduğu gözlenmiştir. SO_x türleri ve NO_x türlerinin aynı anda var olduğu durumda, katalizör yüzeyindeki aktif bağlanma noktalarına dair rekabeti, SO_x türlerinin belirgin bir üstünlükle kazandığı saptanmıştır. Perovskitlerin kristal örgülerindeki oksijen miktarı, oksijen boşlukları ve indirgenme profilleri; B-bölgesindeki kompozisyona bağlı olarak farklılıklar göstermektedir. Perovskit kristal örgüsündeki, Co-O bağlarının, yapıdaki artan Mn yüklemesiyle birlikte, Mn-O bağlalarıya yer değiştirdiği, ex-situ FTIR deneyleriyle gösterilmiştir. Hibrit perovskitlerin spesifik yüzey alanları, yapıdaki Mn yüklemesinin artırılmasına bağlı olarak artmaktadır. Mevcut çalışmalar çerçevesinde elde edilen deneysel sonuçlar; hibrit perovskitlerin yüksek NO_x depolama kapasitesi ve yüksek SO_x toleranslarına sahip olduklarını ve yapılarının sentetik olarak kontrol edilmesiyle, yüzey kimyasal özelliklerinin, redox davranışlarının, NO_x/SO_x türleriyle etkileşimlerinin değiştirilerek, yüksek performansa sahip, özgün De-NO_x katalizörlerinin tasarımına olanak verdiğini göstermektedir.

Anahtar sözcükler: Perovskit, NO_x, SO_x, $LaMnO_3$, $LaCoO_3$, $LaCo_xMn_{1-x}O_3$

Acknowledgement

First, I would like to thank Assoc. Prof. Dr. Emrah Özensoy for his continuous support of my Ms. study and related research, for his motivation and great knowledge. His guidance motivated me to be a part of his research group and write this thesis. It has been a great pleasure working with him.

I would like to thank Zafer Say for his contributions about spending his valuable time with me during my graduate research.

I also send my thanks to Giuseppe Pantaleo , Anna Maria and Nadia Fichera (CNR- ISMN, Italy) for their collaboration.

I also would like to thank Zehra Aybegüm Samast , Merve Tohumeken, Merve Doğaç Kurt , Mustafa Karatok , Deniz Altunöz Erdoğan, Evgeny Vovk for their scientific contributions and companionship.

I would like to thank Asst. Prof. Dr. Bilge Baytekin and Assoc. Prof. Dr. Okan Esentürk for their important contributions to evaluation process of this study.

I want to thank to TUBİTAK for their financial Support (project code: 213M585). I also would like to pronounce my sincere feelings to Ahmet Uçar, Sinem Gürbüz, Emre Köken, Pelin Altay, Aydın Kahriman, İdris Tuncer Yıldız, Emre Turna, Ali Murat Ünsal, Ezgi Yılmaz, Cansu Kaya, Esra Deniz Soner and Taha Yıldırım for their great support and friendship.

Lastly, I wish to announce my deep gratitude's to my parents; my father Adem Ercan, my mother Meryem Ercan and my sisters Beyza Nur Ercan and Melike Nur Ercan. There are not enough words to express my deep loyalty to them. I could not imagine a life without their existence. I wish them to have long and peaceful life.

“Dedicated

to my sister Melike Nur Ercan”

Contents

List of Figures

List of Tables

List of Abbreviations

BET: Brunauer-Emmett-Teller

EDX: Energy-Dispersive X-ray spectroscopy

FTIR: Fourier Transform Infrared Spectroscopy

ICDD: International Center for Diffraction Database

IR: Infrared

JCPDS: Joint Committee on Powder Diffraction Standards

NIST: National Institute of Standards and Technology

NO_x: N_2O, NO, NO_2

NSR: NO_x Storage and Reduction

NSC: NO_x Storage Capacity

PGM: Platinum Group Metal

PID: Proportional Integral Derivative

RT: Room Temperature

QMS: Quadruple Mass Spectrometer

SCR: Selective Catalytic Reduction

$SO_{x:}$ SO_2+O_2

TCD: Thermal Conductivity Detector

TEM: Tunneling Electron Microscopy

TPD: Temperature Programmed Desorption

TPR: Temperature Programmed Reduction

XPS: X-ray Photoelectron Spectroscopy

XRD: X-Ray Diffraction

Chapter 1

Introduction

1.1.Air Pollution and NSR Technologies

1.1.1. Air Pollution

Air pollution level is one of the leading global problems [1]. In the last decades, environment agencies constantly reduced the toxic gas levels allowed in the atmosphere such as NO_x, SO_x and CO by applying very strict emission regulations. Principally, NO_x emission originates mostly from mobile sources (such as trucks, automobiles etc…), and also contributes to the greenhouse effect [2], [3]. Thus, significant scientific and engineering efforts are currently being conducted in order to design new catalysts that can meet challenging emission regulations.

1.1.2. NO_x Storage Reduction (NSR) Technology

Classical three way catalysts are not efficient in the removal of NO_x under lean burn (i.e. oxidizing) conditions. Hence, alternative technologies have been designed to decontaminate NO_x species under lean-burn conditions. Direct (homogeneous) thermal decomposition of NO (i.e. $NO \rightarrow 1/2N_2 + 1/2O_2$) without a catalyst is feasible, however this process requires relatively high activation energy limiting the reaction kinetics significantly. Selective catalytic reduction

(SCR) is a promising technology to reduce NO_x with hydrocarbons (HC), NH_3 and H_2 under oxidizing conditions. On the other hand, there are certain drawbacks of SCR catalysts associated with the narrow operational temperature range, low structural durability and insufficient activity [4],[5]. Hence, NSR technologies have been developed as a contender technology to meet NO_x emission regulations. NSR systems store NO_x species selectively on the catalyst and subsequently reduce the stored NO_x with the help of excess fuel. NSR systems operate in the exhaust systems in two successive cycles. In the first cycle, engine works under lean (excess oxygen) conditions and NSR catalyst stores NO_x in the solid state. Then, the engine switches temporarily to the rich (leading to reducing agents like HC, H_2, CO) cycle in order to reduce trapped NO_x to N_2 [3]. NSR systems do not require any external reducing agent such as NH_3 (i.e. urea) as in the case of SCR systems. However NSR catalysts reveal various challenges associated with limited sulfur tolerance, high cost for Platinum Group Metals (PGM) and extra fuel penalty originating from rich cycles. Thus, NSR systems need to be optimized by designing catalytic architectures with low cost, high NO_x storage capacity (NSC), high thermal stability and enhanced sulfur tolerance.

1.2.Properties of Perovskites in Relevance to De-NO_x Catalysis

1.2.1. Characteristics of Perovskites

Perovskites have been studied intensely in the heterogeneous catalysis literature since 1970's. Initials studies in the literature showed that perovskites have a significant potential to be used as reduction and oxidation (redox)catalysts

with a potential to replace precious PGM [6]–[9]. More recent studies also showed that perovskites may also be optimized to be utilized in modern NSR systems [10].

Perovskite-based catalysts exist (ideally) in the form of ABO_3 where A and B are metal cations and O is the oxide anion. A is the larger cation which can be an alkaline, alkaline earth or lanthanide cation while B is a transition or post-transition metal cation. In the crystal structure, A and B are found in 12-fold and 6- fold coordination; respectively. Moreover, in the unit cell of perovskites, A cations are positioned in the center, B cations are located on the corners and O^{2-} anions are positioned on the edge-centers (Figure 1) [11].An important aspect of perovskite formulations is the fact that, A and B sites can be filled with hetero-atoms leading to complex formulations such as $A_xA'_{1-x}B_yB'_{1-y}O_{3\pm\alpha}$. These compositional lattice modifications of the perovskites lead to a rich variety of electronic, chemical, optical and thermal alterations not only in their bulk properties but also in their surface characteristics.

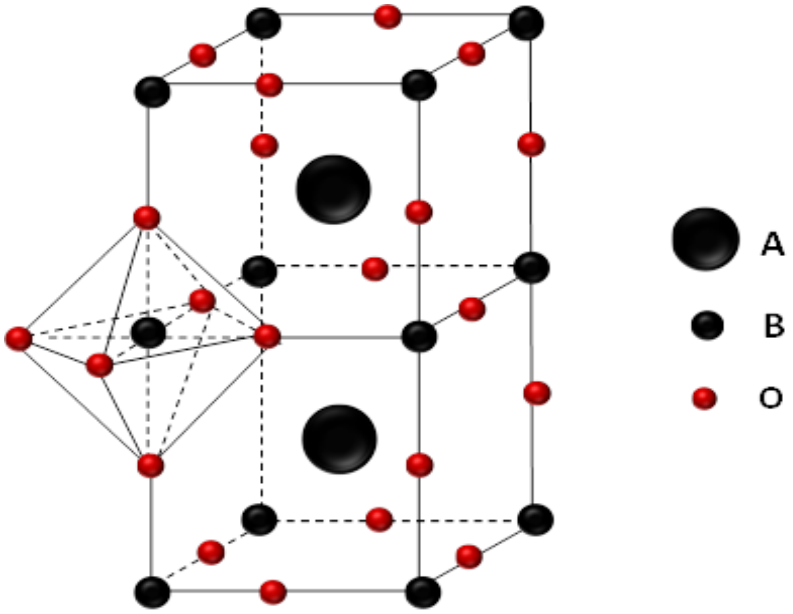

Figure 2. Schematic representation of the cubic perovskite crystal structure [11]**.**

Moreover, stability of the crystal structure is another important issue for the perovskite systems. A-O and B-O bond distances in the unit cell dictate an important factor *"t"* which is given by:

$$t = r_A + r_O / \sqrt{2}\,(r_B + r_O) \quad (1)$$

r_A ,r_B and r_O correspond to the ionic radii of A/B cations and O^{2-} anions in the crystal structure; respectively. *"t"* is a term called the *"tolerance factor"*. Cubic crystal structure is preferred for $0.75 < t < 1.0$. To have an ideal cubic perovskite structure, *t* value should be close to 1, which typically requires high synthesis temperature [11]. On the other hand, insertion of A site cations into the crystal structure may commonly distort the BO_6 octahedron leading to different crystalline phases such as rhombohedral or orthorhombic structures (Figure 2) [12].

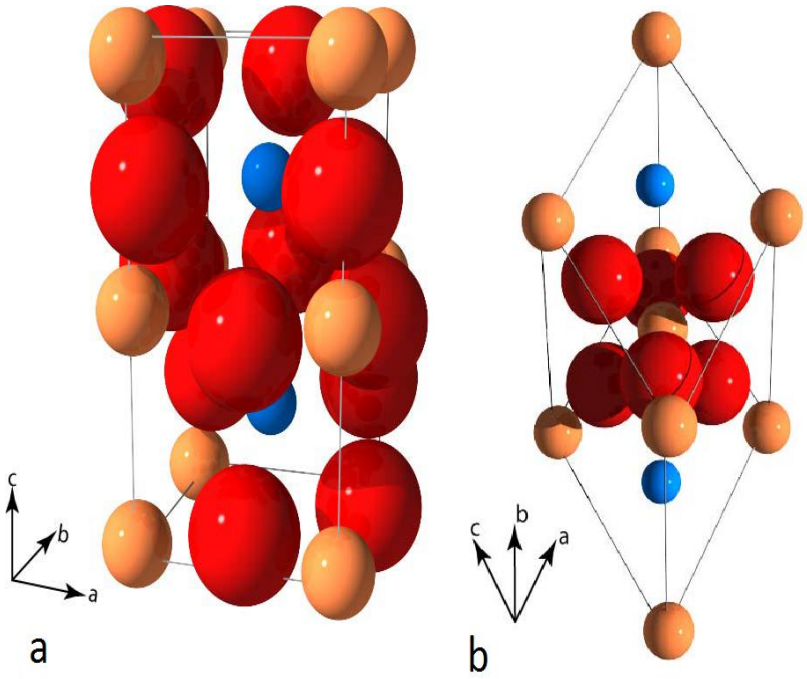

Figure 3. a) Rhombohedral and b) orthorhombic crystal structure of perovskites [12].

1.2.2. Redox Properties of Perovskites

Redox properties of perovskites systems are critical for the catalytic processes. Oxidation states of A and B site can be manipulated by loading different cations. Substitution of the B site have a direct impact on the catalytic properties of perovskites where the effect of A site elements are rather indirect [13]. A-Site cations are surrounded by BO_6 octahedra providing a more stable oxidation state and a relatively weaker redox activity. Catalytic activities of $LnBO_3$ (Ln = rare earth elements) are mostly dictated by the redox properties of B site cations[14], [15]. Futai et al. [16] studied the reduction profiles of $LnCoO_3$ perovskites where Ln is chosen among Pr,Nd,Sm,Eu,Gd,Tb,Dy. Two reduction

peaks were observed at 400 ^{o}C and 625 ^{o}C. Low temperature reduction peak was associated with $Co^{3+} \rightarrow Co^{2+} + e^-$ while the second reduction peak was attributed to $Co^{2+} \rightarrow Co^{0} + 2e^-$ (i.e. metallic cobalt formation). A Similar work was carried out also by Crespin et al. [17] who reported the reduction of perovskites process in the following steps;

$$2LnCoO_3 + H_2 \rightarrow 2LnCoO_{2.5} + H_2O \qquad (1)$$

$$2LnCoO_{2.5} + 2H_2 \rightarrow Ln_2O_3 + 2Co + 2H_2O \qquad (2)$$

As mentioned before, reaction *(2)* represents low temperature partial reduction whereas reaction *(3)* corresponds to the irreversible reduction of Co^{2+} to metallic cobalt. Reduction temperatures of such perovskites were found to be strongly influenced by the calcination temperature used in the perovskite synthesis. Irusta et al.[18] reported that as the calcination temperature increases, reduction temperatures of Co-based perovskites shifted towards higher temperatures for both of the reduction steps. It was argued that as the calcination temperature increases, mean size of crystallite size increases while the specific surface area of the perovskites decreases. These large crystals were suggested to yield higher diffusion barriers for H_2 and thus higher reduction temperatures [19].

Modification (partial substitution or complete substitution) of A site alters the reducibility of the perovskite structure. Using larger ions in the A site of the perovskite systems yields less-reducible structures. In particular, reduction temperature of the Co-based ($ACoO_{3)}$ perovskites with different A site cations increases in the following order Sm<Nd<Pr<La where the larger cations form

more stable structures [20]. Furthermore, binding energy of the core level electrons of the atoms constituting the perovskite lattice is another parameter relevant to the relative redox properties. According to Futai et al, maximum reduction temperature of the Co-based perovskites increases as the O1s binding energy of the surface oxygen species increases. However, there is no direct relation with the size of the A site cation and the binding energy of the surface O1s species where a complex ranking is obtained for the O1s states as a function of perovskite composition : $LaCoO_3$< $PrCoO_3$< $NdCoO_3$< $SmCoO_3$< $EuCoO_3$> $GdCoO_3$> $TbCoO_3$ < $DyCoO_3$ [16]. Partial substitution of A site changes the reduction pattern of perovskites. For instance, incorporation of Sr in $La_{1-x}Sr_xCoO_3$ systems favors the formation of Co^{4+} species as well as oxygen vacancies which in turn, lead to a more reducible structure. Similar work has been done for Mn based ($AMnO_3$) perovskite systems. Sr^{2+} loading in the $La_{1-x}Sr_xMnO_3$ systems also favors the formation of Mn^{+4} [21].

1.2.3. Oxygen Mobility of Perovskites

Oxygen mobility and the vacancy diffusion in perovskites are crucial in their catalytic redox properties. TPD is one of the most common techniques to investigate the oxygen release patterns of perovskites. Perovskites are comprised of numerous different types of oxygen species with various oxidation states, coordination configurations and locations in the unit cell. However, oxygen release from perovskite structures are observed through only two discernible desorption states namely, α-O_2 or β-O_2 states. α-state is associated with surface oxygen species while β-O_2 originate from bulk oxygen species [22]. Weakly

bound oxygen states desorb from the surface at relatively low temperatures (i.e. α-oxygen). On the other hand, β-oxygen is released from bulk at higher temperatures. TPD experiments on $La_{0.99}Co_{0.86}Fe_{0.15}O_{3-o}$ indicate that increasing calcination temperature monotonically shifts the α-O_2 peak to higher temperatures while the total amount surface oxygen reveals a non-monotonic trend where the oxygen release form α-O_2 peak first increases then decreases [23]. In contrast, amount of desorbing β-O_2 species continuously increases with increasing calcination temperature [23] and desorption of β-O_2 is not only desrobed from monolayer (in lattice) but also multiple layers may contribute β-O_2 desroption [19].Teraoka et al. reported that desorption patterns of α-O_2 and β-O_2 states are interconnected to the defect properties of perovskites [24].Furthermore, partial substitution of Sr^{2+} was found to enhance the desorption of α-O_2 released from Co-based perovskites. Desorption of β-O_2 leads to the reduction of the transition metals (i.e. B-site cations) to lower oxidation states [24]–[26].Furthermore, α-O_2 desorption in $La_{1-x}Sr_xCoO_3$ was observed to closely depend on the oxygen vacancy density which can be modified by varying Sr loading as x=0.4, 0.6 [27], [28].Isotopic exchange using $^{16}O/^{18}O$ is also another important technique to study oxygen mobility. $La_{1-x}Sr_xCoO_3$ type perovskites were found to accept gaseous ^{18}O into the lattice. Low loadings of Sr^{2+} does not affect the exchange rate of $^{16}O/^{18}O$ at low temperatures such 150 ^{0}C; however exchange rate drastically increases at higher temperatures (e.g. 300 ^{0}C) [28]. Excessive Sr^{2+} substitution of $La_{1-x}Sr_xCoO_3$ such as x=0.6 enhances the exchange rate even at low temperatures (i.e. 150 ^{0}C) [28]. Nakamura et al. concluded that Sr^{2+} substitution resulted in the enhancement of oxygen vacancies and raised the oxygen mobility from surface to

bulk [28]. Nitadori et al. indicated that oxygen adsorption capacity depended on the oxygen vacancy, oxidation states of A and B sites, revealing a strong influence on catalytic reactivity [29]. Royer et al. showed that morphological structure of the perovskites could be important for oxygen mobility. They demonstrated that materials with comparable chemical compositions may show different oxygen mobility due to unlike crystallite size [30]. Yang et al. reported that there are dissociation and adsorption of gas phase oxygen and diffusion may follow two major pathways namely, (i) direct diffusion to the bulk or (ii) diffusion into the grain boundaries [31].

1.2.4. Surface Acidity of Perovskites

Surface Acidity is a key parameter to identify interaction between NO_x species and perovskite surfaces. NO_x species are acidic species therefore; decreasing surface acidity of perovskites strengthens the NO_x adsorption under operational conditions. However, extremely high surface acidity weakens the NO_x adsorption strength and thus the NSC. Therefore, an optimum surface acidity is needed to enhance the NO_x storage and reduction properties of perovskites. CO adsorption performed under ambient conditions revealed a vibrational feature at around 2058 cm^{-1} which is independent of the La/Co ratio [32]. Centers of Lewis Acid sites with CO interaction which are detected by IR signals as carbonate species assigned in between 1250-1750 cm^{-1} [33]–[35] are distributed on the surface of perovskites and this interaction disappears at higher temperatures hence spectral bands shift to higher wave numbers 2280-2400 cm^{-1} which are related CO_2 species where the temperature higher than 150 ^{O}C [32]. Kuhn and

Ozkan et al. studied the surface properties of cobaltites in the form of $La_{0.6}Sr0._4Co_yFe_{1-y}O_{3-\delta}$ with y=0.1, 0.2 and 0.3. Their results suggested that amount of basic sites were proportional to the Co content. Substitution of La^{3+} with Sr^{2+} altered the charge balance in the lattice and produce acidic sites [36]. However, Natile et al. confirmed that the acidic character of $LaCoO_3$ is promoted by La^{3+} as well as Co^{3+} [32]. Besides, Kuhn and Ozkan et al. also reported that it is difficult to oxidize surface Co ions as compared to Fe ions leads to the (Co enrich surface) formation of intense oxygen vacancies and allows rapid diffusion of oxygen into the lattice , means that based on number of oxygen defect sites Co ions are increasing the surface acidity [36]. $LaMnO_{3+y}$ type perovskites were suggested to be basic perovskites [37]. Density functional theory calculations and CO_2 adsorption were used to identify the surface basicity of $LaMnO_{3+y}$.These former experiments demonstrated that CO_2 adsorption was weak on the MnO^{2-} terminated surface. The strongest adsorption on La cations was correlated with the presence of F_s-centers. As a result, adsorptions on cationic sites resulted by weak basic sites [37].

1.2.5. General View of Oxidation Reactions on Perovskites

In the perovskite structure (ABO_3), B site cations, which are the catalytically active sites, typically come along with two different oxidation states (i.e. +2 and +3). $LnBO_3$ perovskites where Ln corresponds to lanthanum and B corresponds to Mn, Ni, Fe, or Co are known to be some of the most active perovskites for CO oxidation reactions [11]. However, H_2 bond activation or CH_4

oxidation (Figure 3) is not effective at low temperatures on such perovskites as compared to noble metals (e.g. Pd) dispersed on conventional metal oxides.[38].

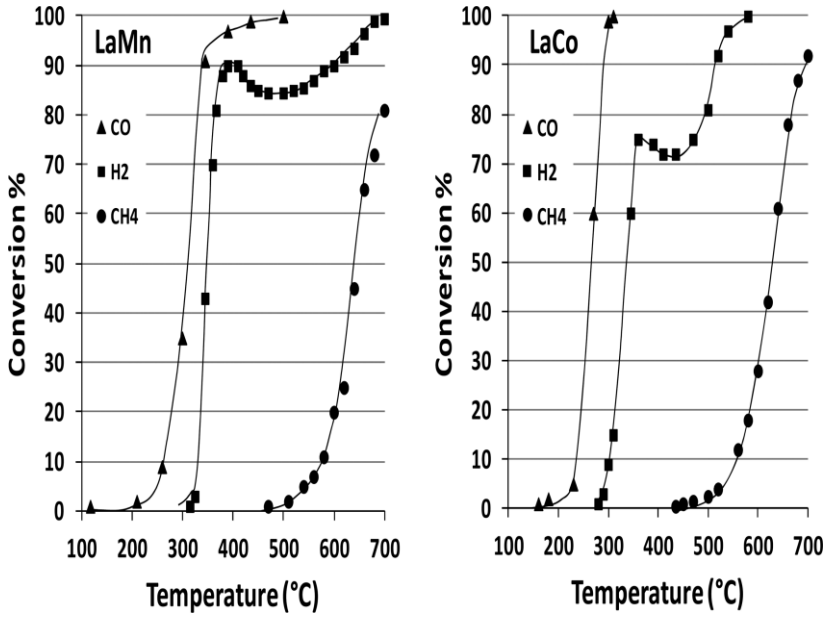

Figure 4. Catalytic oxidation process of H_2, CO and CH_4 upon $LaMnO_3$ and $LaCO_3$ [38].

There are two different mechanism defined for the oxidation reactions over perovskites. *Suprafacial* mechanism is considered for low temperature oxidation reactions which involves the utilization of exclusively surface oxygen species. In contrast, the so called *intrafacial* mechanism is typically valid for high temperatures and includes the migration of oxygen ions that migrate from bulk to surface. This latter process resembles to the Mars van Krevelen mechanism [39]. Furthermore, in the methane oxidation process over the $La_{1-x}M_xMnO_{3+\delta}$ catalyst, where M can be either Sr or Ce, catalytic activity of oxidation was found to be closely correlated with the number of Mn^{4+} ions, more specifically to the number

of –O-Mn^{3+}-O-Mn^{4+} linkages [40]. A related study also suggested that addition of Sr^{2+} ions enhanced the oxidation Mn^{3+} to $Mn^{4+}$and increased the catalytic activity for methane oxidation [41]. In addition Oliva et al. [40] reported that Mn^{4+} population and the oxygen mobility in the perovskite structure can increase due to the reduction of Mn^{3+} sites into Mn^{2+} which can strongly alter the reactivity.

1.2.6. NO_x Decomposition on Perovskites

Numerous studies have been carried out on the NO_x abatement in automotive applications with perovskites [10]. In the forth coming section, catalytic decomposition of various NO_x species such as N_2O and NO in relevance to exhaust emission catalysis will be discussed in detail.

1.2.6.1 N_2O Decomposition

One of the commonly proposed mechanism in the literature suggests that N_2O decomposition has closely related to the oxygen mobility as shown in equations*(4-6)* given below[42].

$N_2O + * \leftrightarrow N_2O*$ *(3)*

$N_2O* \rightarrow N_2 + O*$ *(4)*

$2O* \leftrightarrow O_2 + 2*$ *(5)*

In the N_2O decomposition mechanism shown above, asterisk "*" represents the active site for N_2O adsorption. N_2O decomposition starts with N_2O adsorption on surface oxygen and leads to the formation of N_2. Ivanov et al.

showed that the N_2O decomposition activity of $La_{1-x}Sr_xMnO_3$ (where x was varied between $0 \leq x \leq 0.7$) [43], [44] increased with oxygen mobility characteristics. Oxygen desorption was reported to be the rate determining step for N_2O decomposition which also strongly depended on the surface O1s binding energy of oxygen [45]–[47]. On the other hand, oxygen mobility is not the only parameter for N_2O decomposition; synthesis routes leading to higher SSA for $LaCoO_3$ and Pd impregnation to $LaCO_3$ also increase the N_2O decomposition activity of perovskites [48], [49].

1.2.6.2 NO Decomposition

Direct NO decomposition is another important process to remove NO_x species as it does not require an additional reducing agent. B site coordination with oxygen species result in (Figure 4) B-O (T') square, B-O (T*) pyramidal and/or B-O (T) octahedral coordination. Oxygen vacancies in B-O pyramids favor the oxygen mobility and former reports confirm that active sites for NO decomposition is comprised of two adjacent oxygen vacancy sites (i.e. Route *a*) or one lattice oxygen in between two transition metal sites (Route *b*) [50], [51].

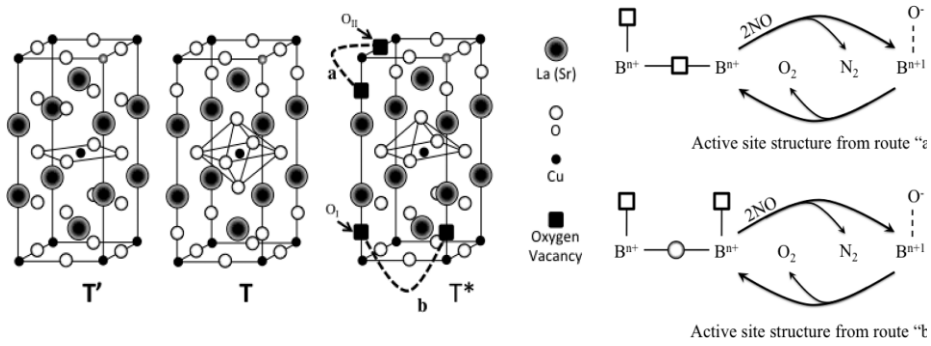

Figure 5. Crystal structure of perovskites in the form A_2BO_4 with active sites for NO decomposition (T′, T, and T*) and possible routes (a,b) [51].

$La_{0.4}Sr_{0.6}Mn_{0.8}Ni0_{.2}O_3$ type of perovskite was studied to elucidate the kinetics and mechanism of NO decomposition [52]. It was stated that N_2 formation is monotonically proportional to the NO partial pressure, however oxygen partial pressure revealed a negative order where increasing oxygen partial pressure decreased the rate of NO decomposition [53]–[55]. Furthermore, Tofan et al. indicated that oxygen inhibition alters accordingly temperature and material composition since oxygen blocks regeneration of active sites [56]. To illustrate the material composition effect, Ishihara et al. studied $LaBO_3$ materials where B was chosen as Mn, Co, Cu, Fe and Cr [57]. It was identified that the direct NO decomposition activity increased in the following order: Mn>Co>Cu>Fe >> Cr. On the other hand, Iwakuniet al. reported the effect of material composition by using $BaMnO_3$ perovskites and results showed that direct NO decomposition decreased in the following order: Mg >Zr> Fe > Ni > Sn > Ta when these species substituted with Mn in the perovskite structure [54].

1.2.7. NSR Systems Utilizing Perovskites

As mentioned above, NSR systems have been widely studied since 1990s [58]–[62]. NO_x trap catalysts usually include a noble metal (Pt), providing NO oxidation and H_2 bond activation. Additionally, they contain a storage component such as barium oxide and a support material such as alumina [2]. However, high cost of precious metals and sulfur sensitivity of storage component [63], [64] are critical drawbacks of NO_x trap catalysts. On the other hand, perovskites are promising candidates for NSR catalysis due to their reasonable NO_x storage efficiency and low cost.

Kiennemann et al. studied a series of perovskites by using a complex gas mixture (NO, NO_2, CO, O_2, H_2O) and pointed out that $BaSnO_3$ was the most promising catalyst for NO_2 oxidation and storage [65]. However, this particular material was not efficient for NO oxidation and addition of Pt led to only a minor improvement. Although the presence of CO_2 strongly influenced the NSC of $Pt/Ba/Al_2O_3$ benchmark catalyst [66], [67], $BaSnO_3$[65] was not affected by CO_2. SO_2 exposure over the catalysts results in the formation of irreversible bulk sulfates, decreasing the NSC of $BaSnO_3$ [68]. Furthermore, NO_x storage properties of $BaFeO_3$ and $BaCeO_3$ were also studied which showed higher NO_x storage capacity as compared to $BaSnO_3$ [69]. To increase the NO_x storage capacity of $BaCeO_3$, Pt and Rh addition was investigated [70], however it was found that NSC values decreased upon PGM addition. On the other hand, $BaCeO_3$ and $BaFeO_3$ show resistance for sulfur poisoning and NSC of $BaCeO_3$ is not affected from SO_2 exposure [70]. It was argued that the presence of iron inhibited the sulfate

formation [71]. On the other hand, it is reported that SO_x and NO_x removal efficiency (dosed at the same time) is %90 and %98 for NO and SO_2 respectively indicate that $LaCoO_3$ has inherent resistance for SO_x [72]. High sulfur tolerance and high NO_x storage capacity were observed for $BaCo_{0.6}Fe_{0.4}O_{3-x}$ perovskites which exceeded that of the $Pt/BaO/Al_2O_3$ benchmark catalyst [73]. Furthermore, $La_{0.9}K_{0.1}Co_{1-x}Fe_xO_{3-y}$was the subject for another study and results showed that high catalytic activity was connected to the Fe^{4+} species and the amount of surface oxygen [74]. Besides that Sr-substituted $La_{1-x}Sr_xCoO_3$ type perovskites were found to reveal promising activity in the oxidation of NO to NO_2 [10].

NO_x oxidation and reduction cycles are considerably important for perovskites as the perovskite structure should not be reduced irreversibly while NO_x is reduced to N_2. There are multiple reports indicating that perovskite structure can be maintained after reduction of nitrate species under lean conditions at ca.400 ^oC [75]. Moreover, $La_{1-x}Sr_xCoO_3$ type perovskites reveal performances close to commercial platinum-based DOC catalysts in terms of NO_x storage and reduction capacity and they can even yield better performance in the presence of sulfur [10].

Chapter 2

Experimental

2.1.Sample Preparation

2.1.1. Synthesis of Simple $LaMnO_3$ and $LaCoO_3$ Perovskites

The citrate method has been used to synthesize simple $LaCoO_3$ and $LaMnO_3$ perovskites based on the synthesis route described in a patent of General Motors Company [76]. First, amount of precursors were determined for the synthesis of a 1 g perovskite sample (Table 1). Citric acid amount was determined by multiplying molecular weight of citric acid and total mole number of La, Mn or/and Co with %10 mass percent citric acid excess then it was dissolved in deionized water. After addition of citric acid, nitrate based precursors of La, Mn or Co were added into the solution. Solution was stirred for 1 hr under ambient conditions. Then, the solution was heated up to 353 K during constant stirring. Heating process was continued until the gel formation was obtained. This is followed by the drying process. The gel was dried at 363 K under ambient conditions for 24 hr. After the drying process solid particles were ground to obtain a fine powder. Finally, powder sample was calcined at 973 K in air for 5 hr.

2.1.2. Synthesis of $LaCo_xMn_{1-x}O_3$ Type Hybrid Perovskites

Synthesis of $LaCo_xMn_{1-x}O_3$ hybrid perovskites were performed using a similar method as described in section 2.1.1 with the exception that Co and Mn precursors were added to the solution simultaneously by using "x" values varying within $0.1 \leq x \leq 0.9$ (Figure 5). The precursor amounts used in the synthesis are listed in Table 2.

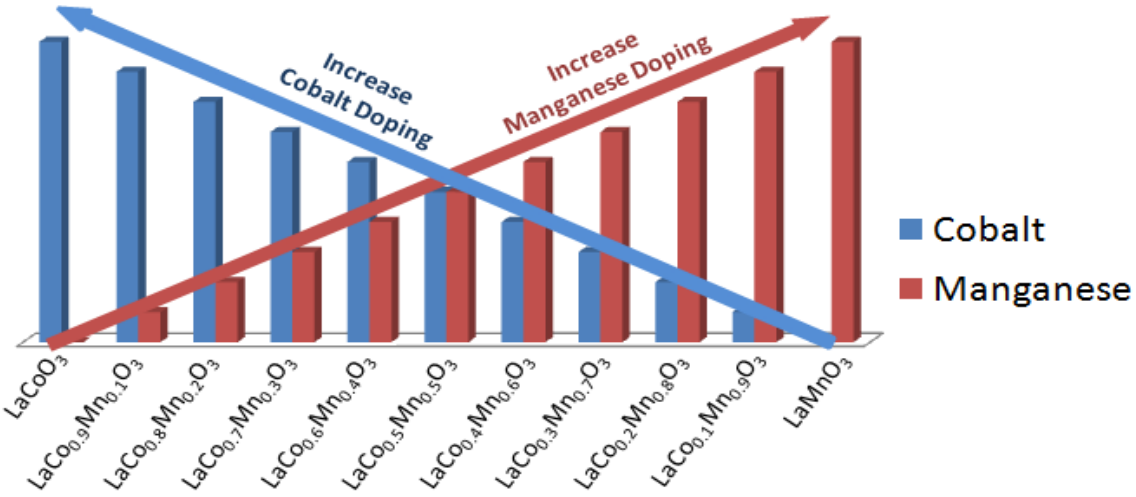

Figure 6. Schematic representation of the compositional variation of hybrid perovskites.

Table 1. Amount of precursors used in the synthesis of simple perovskites

Precursors	**$LaMnO_3$**	**$LaCoO_3$**
$La(NO_3)_3.6H_2O$	1.7905g	1.7613g
$Mn(NO_3)_3.4H_2O$	1.0379g	-
$Co(NO_3)_2.6H_2O$	-	1.1838g
Citric acid	1.9116g	1.8805g
Distilled water	82.7ml	81.3ml
Calcination Temperature	973 K	973 K

Table 2. Amounts of materials used in the synthesis of hybrid perovskites.

Precursors	**$LaCo_{0.1}Mn_{0.9}O_3$**	**$LaCo_{0.2}Mn_{0.8}O_3$**	**$LaCo_{0.3}Mn_{0.7}O_3$**	**$LaCo_{0.4}Mn_{0.6}O_3$**	**$LaCo_{0.5}Mn_{0.5}O_3$**
$La(NO_3)_3.6H_2O$	1.7875 g	1.7846 g	1.7816 g	1.7787 g	1.7758 g
$Mn(NO_3)_2.4H_2O$	0.9326 g	0.8276 g	0.7229 g	0.61866 g	0.5147 g
$Co(NO_3)_2.6H_2O$	0.1201 g	0.2398 g	0.3592 g	0.47819 g	0.5967 g
Citric Acid	1.9085 g	1.9022 g	1.9022 g	1.8990 g	1.8959 g
Distilled Water	82.5833 ml	82.4485 ml	82.236 ml	82.1759 ml	82.0422 ml
Calcination Temperature	973K	973K	973K	973K	973K
Precursors	**$LaCo_{0.6}Mn_{0.4}O_3$**	**$LaCo_{0.7}Mn_{0.3}O_3$**	**$LaCo_{0.8}Mn_{0.2}O_3$**	**$LaCo_{0.9}Mn_{0.1}O_3$**	----
$La(NO_3)_3.6H_2O$	1.7729 g	1.7700 g	1.7671 g	1.7639 g	----
$Mn(NO_3)_2.4H_2O$	0.4110 g	0.3078 g	0.2049 g	0.10225 g	----
$Co(NO_3)_2.6H_2O$	0.7149 g	0.8328 g	0.9502 g	1.0669 g	----
Citric Acid	1.8929 g	1.8898 g	1.8867 g	1.88325 g	----
Distilled Water	81.9078 ml	81.7748 ml	81.6407 ml	81.4918 ml	----
Calcination Temperature	973K	973K	973K	973K	----

2.2.Instrumentations

2.2.1. XRD Patterns

Perovskite XRD patterns were recorded from the powder samples by using a Rigaku diffractometer equipped with a Miniflex goniometer. Standard X-Ray source has been used with a Cu Kα radiation at λ=1.5418 Å kV and 15 mA. Powder samples were placed on quartz slides and pressed. Perovskite samples were scanned in the 2θ range of 10-80^{o} with a scan rate 0.01 deg.s^{-1}. Assignment of diffraction patterns were executed by using Joint Committee on Powder Diffraction Standards (JCPDS) cards provided by the International Centre for Diffraction Database (ICDD).

2.2.2. BET Measurements

The specific surface area measurements were performed by using the five-point Brunauer-Emmett-Teller (BET) method [77]. The samples were initially evacuated under vacuum for 1hr at RT. Evacuated samples were then heated for 2 hr at 573 K to evacuate the pores of the catalysts. Micromeritics ASAP 2000 gas sorption and porosimetry system was used for performing the BET measurements.

2.2.3. TEM Imaging and EDX Mapping

For the TEM-EDX sample preparation, ground powder samples were spread over a lacey-type carbon film on a copper TEM grid using ethanol as the suspension medium. TEM measurements were performed in the bright-field mode

using a FEI Tecnai G2 F30 microscope with a resolution of 0.17 nm, a Gatan slow-scan CCD camera, and a Gatan serial energy loss spectrometer. 300 keV e-beam acceleration voltage was used for imaging. For elemental analysis of the imaged samples, EDX was performed with 100 keV incident electron energy. EDX acquisition time was around 15-20 s.

2.2.4. XPS Measurements

A SPECS XPS spectrometer was used to collect photo emission data of the perovskites samples. This spectrometer was equipped with a monochromatic Al, Kα, X-Ray irradiation with hν = 1486.74 eV, 400 W and PHOIBOS-DLD energy analyzer. Powder samples were placed on a conducting copper sticky tape for measurement. An electron flood gun was used to prevent surface charging.

2.2.5. Ex-situ Infrared Measurements

Ex-situ infrared measurement data were collected by using a Bruker Tensor 27 infrared spectrometer. Experiments were carried out in transmission mode with a resolution of 4 cm^{-1} and 64 scans/spectrum. Before the ex-situ IR measurements catalyst samples were mixed with KBr using a mass ratio 200 mg /2 mg.

2.2.6. In-situ Infrared Measurements

In-situ experiments have been carried out using an FTIR (Bruker Tensor 27) spectrometer coupled to a quadruple mass spectrometer (QMS, Stanford Research Systems, SRS RGA200) and a custom-made spectroscopic transmission FTIR cell. All in-situ FTIR spectra were collected at 323 K. Catalysts placed in the spectroscopic cell were heated using a linear heating system including an adjustable power supply and a computer-controlled PID controller (Gefran 600-DRRR). Linear heating was applied between 323-1023 K with a heating rate of 12 K/min. A liquid nitrogen-cooled MCT (Hg-Cd-Te) mid-IR detector was used for collecting FTIR data. Pressures of dosed gases were controlled by MKS Baratron Pressure Transducer Type 626 and a wide range pressure gauge (EDVAC WRG-S-NW35) comprised of Piranyi and cold-cathode gauges. FTIR spectra were acquired with a resolution of 4 cm^{-1}. 128 scans were used for each spectrum. Vacuum inside the spectroscopic reactor, gas manifold and dosing lines were obtained via rotary and turbomolecular pumps. Lithographically etched, high purity and high conductivity tungsten grid (TechEtch, USA, P/N PW10379-003) has been used to mount the powder catalyst samples in a self-supported manner which can be heated via resistive heating. For the spectroscopic experiments, samples were prepared within a weight range of 20-45 mg. The sample holder also included a ceramic vacuum feed through with copper legs which is spot-welded to the tungsten. A home-made K-type thermocouple (chromel and alumel with 0.015" radius from Omega Engineering, Inc) was used for temperature measurements where the temperature of the sample could be increased up to 1173

K via the PID controller and DC power supply. Before all experiments, samples were baked out at 403 K for 12 hr in order to remove water and other contaminations from the catalyst surface and eliminate the water from the spectroscopic reactor walls. Also before all experiments, baked catalyst surfaces were exposed to 0.5 Torr NO_2 for 5 min followed by evacuation and vacuum annealing using a linear heating ramp (12/K) up to 973 K.

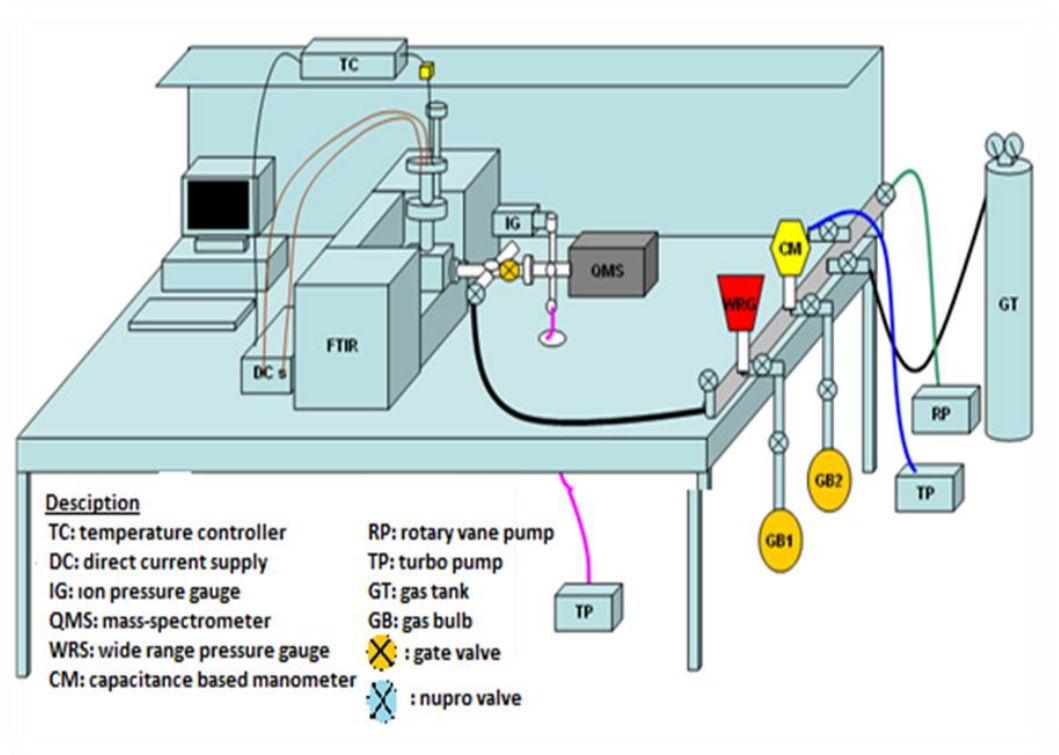

Figure 7. Schematic example of in-situ FTIR and TPD system[78].

2.2.6.1. Stepwise NO_2 Adsorption Experiments

Before NO_2 adsorption experiments, fresh catalyst surfaces were prepared as described in section 2.2.6. Then, 1 Torr NO_2 was dosed to the gas

manifold then released over the sample for 1 min during which the gas pressure of the catalyst sample was observed to be 0.1 Torr due to the expansion of the gas. Before taking IR spectra, chamber was evacuated to10^{-3} Torr. This procedure was repeated 10 times for all stepwise NO_x adsorption experiments. After stepwise adsorption, surface was saturated with 5 Torr NO_2 for 10 minutes. During all of these treatments, sample temperature was held constant at 323 K. NO_2 preparation has been carried out by mixing NO (g) (Air Products, 99.9%) and O_2(g) (Linde GmbH, Germany, 99.999%). Prepared gas mixture was further purified by freeze-pump-thaw cycles using liquid nitrogen.

2.2.6.1. NO_2 Adsorption Experiments over Reduced Perovskite Surfaces

NO_2 adsorption over reduced surfaces was performed by heating the catalysts to 623 K in the presence of 5 Torr H_2(g) for 10 min. After evacuation at 623 K, samples were cooled to 323 K then catalyst surfaces were saturated with 5 Torr NO_2 for 10 min followed by evacuation and FTIR spectrum acquisition.

2.2.6.2. SO_x Adsorption and Reduction via H_2

SO_x adsorption experiments were performed on hybrid and simple perovskites using a SO_2(g)+O_2(g) gas mixture with a partial pressure ratio of 1/10, respectively. In these experiments, after the initial catalyst pretreatment as described in earlier sections, 2 Torr SO_x was dosed over the sample for 10 min and the spectrum was recorded at 323 K. After taking the first spectrum, the sample was heated up to 373-673 K with 100K increments and after each temperature increment; the sample is kept at this temperature 10 min in the

presence of SO_x followed by cooling the sample to 323 K for spectral acquisition. SO_x regeneration process via hydrogen was performed after the evacuation of SO_x gas and subsequent dose of 2.5 Torr H_2(g) into the manifold followed by expansion over the catalyst sample, resulting in a final pressure of 0.5 Torr. After 10 min of hydrogen exposure at 373 K, FTIR spectrum was acquired in the presence of H_2. Then, IR spectra were recorded by heating the sample to various temperatures and cooling back to 323 K in the presence of H_2.

2.2.6.3. SO_x and NO_x co-Adsorption over Perovskites

Pretreated catalyst surface was saturated with 5 Torr NO_2at 323 K for 10 min and the spectrum was recorded. After saturation with NO_2, sample was linearly heated in vacuum to 973 K to remove all of the NO_x species on the surface. Then a SO_2+NO_2 mixture with a SO_2:NO_2 partial pressure ratio of 1:5 (SO_2:O_2:NO_2= 1:10:55) was prepared by pre-mixing the gases for 10 min in the gas manifold. After dosing the gas mixture, catalyst was allowed to equilibrate with the gas for 10 min at 323 K and the spectra were at 323 K in the presence of the gas mixture. Additional spectra were also obtained by heating the catalyst in the gas mixture at 373, 473, 573 and 673 K and then cooling to 323 K in the gas mixture.

2.2.7. TPD Experiments

A Quadruple Mass Spectrometer (QMS) was used to follow desorption patterns of adsorbates on perovskites with a computer controlled linear heating

rate of 12K/min. Before each TPD experiment, QMS filament (made of thoria-coated iridium) was outgassed for 40 min. Up to 11 different desorption channels (i.e. different m/z values) were monitored for different type of experiments. Vacuum level of the TPD reactor was followed by a Bayard-Alpert type ionization gauge with a NEW Granville Phillips 350 UHV Ultra High Vacuum Hot Cathode Ion Gauge Controller. The maximum temperature that could be obtained via the current TPD heating setup was ca. 1073 K.

2.2.7.1. NO_x TPD Experiments over Fresh Perovskites

NO_x TPD experiments were performed after stepwise NO_x adsorption experiments. TPD desorption patterns were recorded after completely opening the that gate valve in between IR and TPD systems in order to allow a direct line-of sight access of desorbing molecules to the QMS ionizer. Then the sample was outgassed for 40 min using the differential pumping provided by the turbomolecular pump located in the QMS vacuum chamber. During the NO_x TPD experiments following m/z desorption channels were recorded: 28 (N_2 or CO), 14 (N), 16 (O), 32 (O_2), 18 (H_2O), 30 (NO), 44 (N_2O), 46 (NO_2).

2.2.7.2. NO_x TPD Experiments over Reduced Perovskites

NO_x TPD experiments for reduced samples were performed after NO_x adsorption experiments over reduced perovskite samples. The procedure that was employed in these experiments was similar to the one described in section 2.2.7.1 with the exception that the catalysts were initially reduced with hydrogen before NO_x saturation.

2.2.8. O_2 TPD Experiments over Perovskites

O_2 TPD experimental procedure consisted of 0.5 Torr NO_2 exposure over the fresh perovskite sample for 5 min and subsequent evacuation. Then, the sample was annealed to 973 K. This initial procedure was used to clean the surface contaminations. However, possible reduction of the surfaces upon the vacuum annealing at 973 K was prevented using a second oxidation step. Thus, prior to the TPD experiment, sample was oxidized for the second time in 10 Torr oxygen for 10 min at 773 K. Then the sample was cooled in oxygen to 323 K and then oxygen gas was evacuated at 323 K. In the TPD experiments, 32 m/z desorption channel was monitored by QMS with the temperature range of 323-1173 K.

2.2.9. H_2 TPR Experiments over Perovskites

TPR experiments were carried out by using Micromeritics Autochem 2910 apparatus located in CNRS-ISMN, Palermo which included a thermal conductivity detector. A gas flow rate of 50 ml/min was used in the TPR experiments where a %5 H_2/He gas feed was flowed over 100 mg of a catalyst sample. Before the TPR experiments, catalysts were pretreated with %5 O_2/He gas mixture with a flow rate of 50 ml/min at 400 K for 30 min. During the TPR experiments, the reduction process was performed within 323-1273 K with a heating ramp rate of 10K/min.

Chapter 3

Results and Discussion

3.1.Structural Characterization of Perovskites

3.1.1.XRD Analysis of Simple and Hybrid Perovskites

Figure 7 shows XRD patterns of hybrid and simple perovskites. Investigation of crystal structures point out that $LaCoO_3$ calcined at 973 K can be assigned to a rhombohedral (ICDD Card No: 00-009-3358) structure in agreement with former reports [10], [79]. $LaMnO_3$ calcined at 973 K corresponds to a cubic (ICDD Card No: 00-052-1099) crystal structure [80], [81].

Table 3. Average Particle Size Calculation of $LaCo_xMn_{1-X}O_3$ perovskites by using Scherrer equation via XRD data.

Sample Name	Full-Width Half Maxima (^{o})	Peak Position (^{o})	D_c Average Particle Size(Voigt)
$LaMnO_3$	0.18	46.85	50.9 nm
$LaCo_{0.1}Mn_{0.9}O_3$	0.15	46.65	59.0 nm
$LaCo_{0.2}Mn_{0.8}O_3$	0.20	46.70	45.2 nm
$LaCo_{0.3}Mn_{0.7}O_3$	0.24	46.63	37.9 nm
$LaCo_{0.4}Mn_{0.6}O_3$	0.22	46.87	40.4 nm
$LaCo_{0.5}Mn_{0.5}O_3$	0.37	46.86	24.8 nm
$LaCo_{0.6}Mn_{0.4}O_3$	0.65	47.07	14.0 nm
$LaCo_{0.7}Mn_{0.3}O_3$	0.61	47.19	14.9 nm
$LaCo_{0.8}Mn_{0.2}O_3$	0.36	47.25	25.2 nm
$LaCo_{0.9}Mn_{0.1}O_3$	0.22	47.36	41.0 nm
$LaCoO_3$	0.19	47.43	47.1 nm

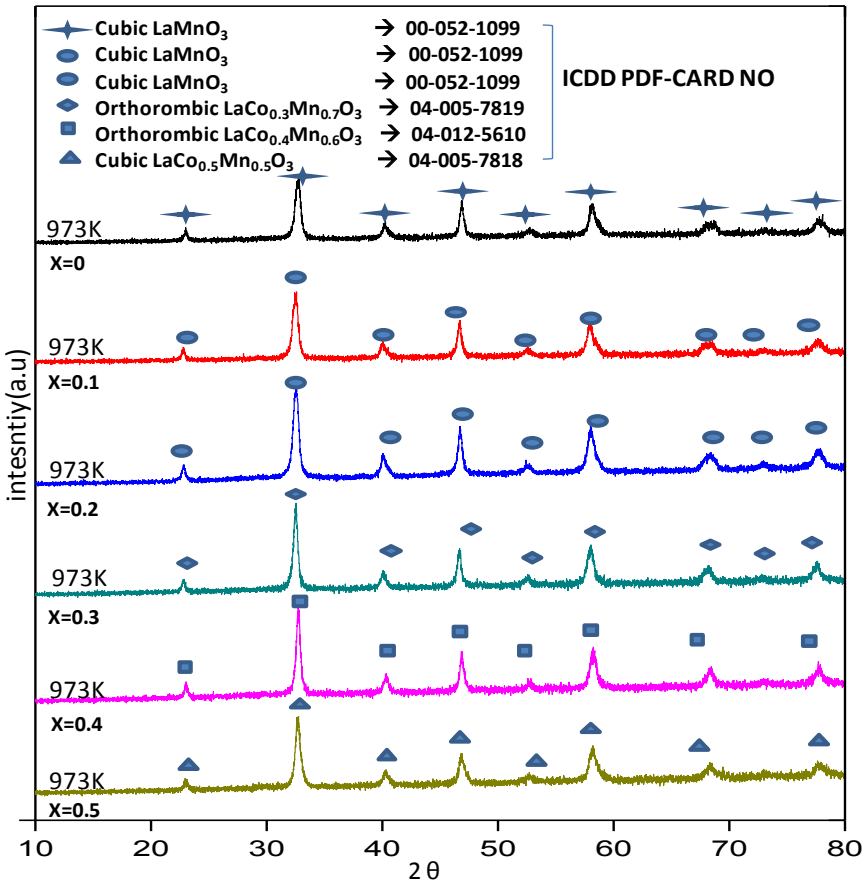

Figure 8.XRD patterns of $LaCo_xMn_{1-X}O_3$ type perovskites x= 0.0-0.5 calcined at 973 K

As it is seen in the Figure 7, cubic structure is still maintained for slight addition of Co (x=0.1, 0.2). Additionally, moderate loading of Co (x=0.3, 0.4) gives rise to orthorhombic (ICDD Card No: 04-012-5610, 04-005-7819) perovskite structure. Equal amounts of Co and Mn (x=0.5) leads to the observation of the cubic(ICDD Card No: 04-005-7818) structure [82].

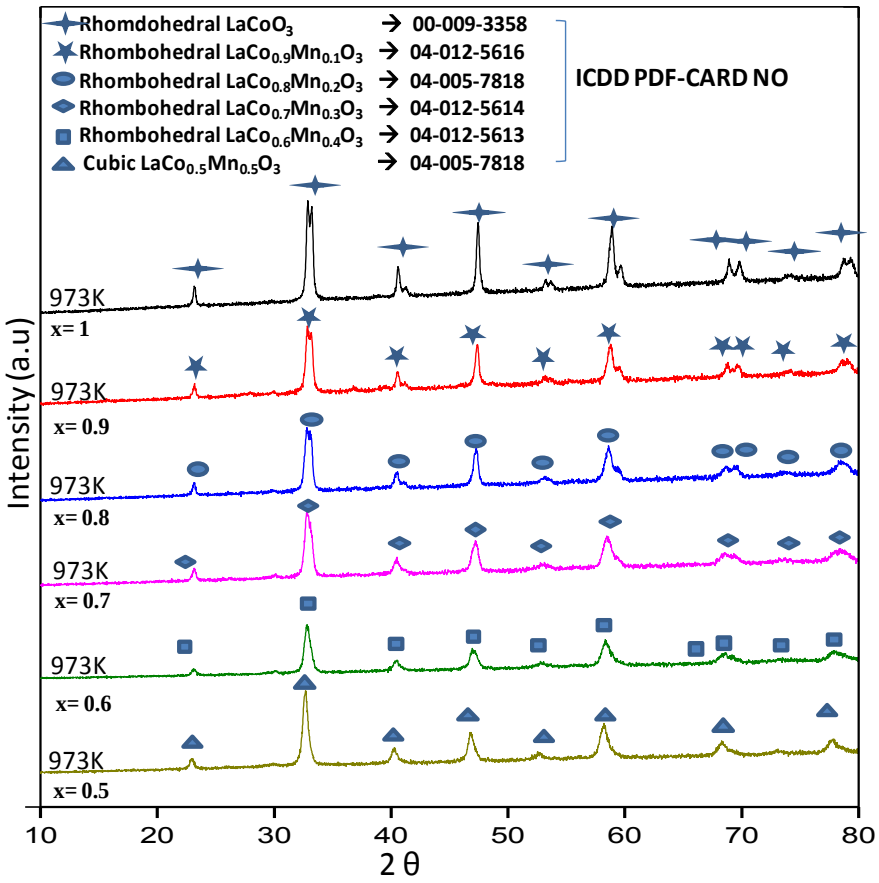

Figure 9. XRD patterns of $LaCo_xMn_{1-X}O_3$ type perovskites x= 1.0-0.5 calcined at 973 K

Figure 8 shows the alteration of the crystal structure as a function of Mn loading. Mn loadings within $0.9 \leq x \leq 0.6$ into the $LaCoO_3$ result in rhombohedral $LaCo_{0.1-0.4}Mn_{0.9-0.6}O_{3\pm y}$ crystal systems. There is no monotonic relationship between the Mn loading and the crystal structure. However, Provendier et al. reported that the shift in the main perovskite peak (2θ=32 to 2θ=33.5) changed monotonically with the extent of Mn loading (i.e. substitution). Average particle size of the synthesized hybrid perovskites, D_c, can be estimated using Scherrer equation [83] as listed in Table 3 where it is seen that the average particles size

varies within ca. 20-60 nm. Particle size is getting smaller owing to small addition of Co (x=0.3, 0.4) then decreases. Diffraction patterns of perovskites are fitted by using voigt function [84]. Average particle size calculations demonstrate that there is no monotonic relationship between B-site composition and particle size.

Finally, XRD patterns suggest that beside these various forms of perovskite polymorphs, no other detectable crystalline phases exist in the synthesized catalytic structures.

3.1.2. BET Analysis of Hybrid and Simple Perovskites

Specific surface area (SSA) results obtained from BET measurements are given in Table 4 and Figure 9 where each perovskite sample was measured 3 times to obtain a statistically representative value. SSA of the currently

synthesized $LaMnO_3$ and $LaCoO_3$ were in very good agreement with the former reports [80].

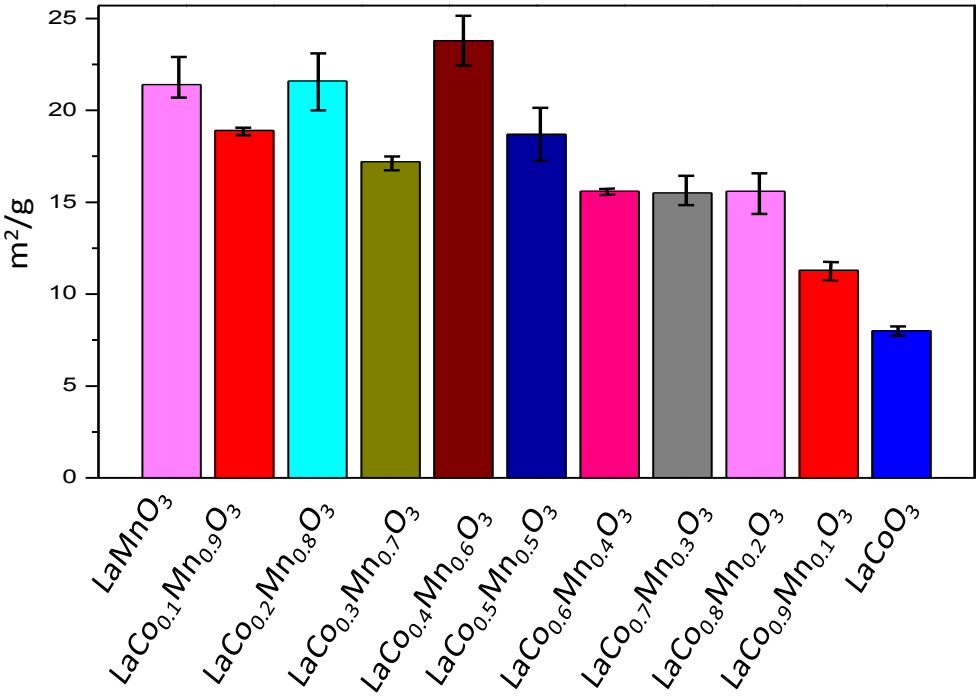

Figure 10. Specific surface area measurements of $LaCo_xMn_{1-x}O_3$ type perovskites (after calcination at 973 K) where x= 0.0-1.0.

In Figure 9, it can be readily concluded that insertion of Mn into the cobaltite structure increases the SSA values. Although the increase in SSA values with increasing Mn loading is monotonic, yet it reveals a complex dependence. Along these lines, it can be argued that the crystallization and ordering of Mn-rich perovskites required higher temperatures compared to that of Co-rich perovskites Thus, Mn-rich perovskites revealed higher SSA values upon calcination at 973 K.

Table 4.SSA values of $LaCo_xMn_{1-X}O_3$ type hybrid perovskites obtained via BET measurements.

Sample Name	**SSA (m^2/g)**
$LaMnO_3$	21.4± 2.2
$LaCo_{0.1}Mn_{0.9}O_3$	18.9± 0.4
$LaCo_{0.2}Mn_{0.8}O_3$	21.6± 3.1
$LaCo_{0.3}Mn_{0.7}O_3$	17.2± 0.7
$LaCo_{0.4}Mn_{0.6}O_3$	23.8± 2.2
$LaCo_{0.5}Mn_{0.5}O_3$	18.7± 2.9
$LaCo_{0.6}Mn_{0.4}O_3$	15.6± 0.3
$LaCo_{0.7}Mn_{0.3}O_3$	15.5± 1.6
$LaCo_{0.8}Mn_{0.2}O_3$	15.6± 2.2
$LaCo_{0.9}Mn_{0.1}O_3$	11.3± 1.0
$LaCoO_3$	08.0± 0.5

3.1.3. TEM Imaging and EDX Analysis

TEM images of $LaCo_{0.8}Mn_{0.2}O_3$, $LaCo_{0.5}Mn_{0.5}O_3$ and $LaCo_{0.2}Mn_{0.8}O_3$ are given in Figure 10 along with representative EDX measurements for elemental analysis. Based on the high resolution TEM images, perovskites are observed to be well-crystallized. Presence of different unit cell parameters indicates a polycrystalline structure. Elemental compositions obtained via EDX measurements are observed to be in good agreement with the nominal catalyst compositions where Mn-rich perovskites reveal an increase in the corresponding Mn signal in EDX. Average particle size of the perovskites studied via TEM was found to be ca. 50 nm which is in fair agreement with the corresponding estimations obtained via XRD measurements

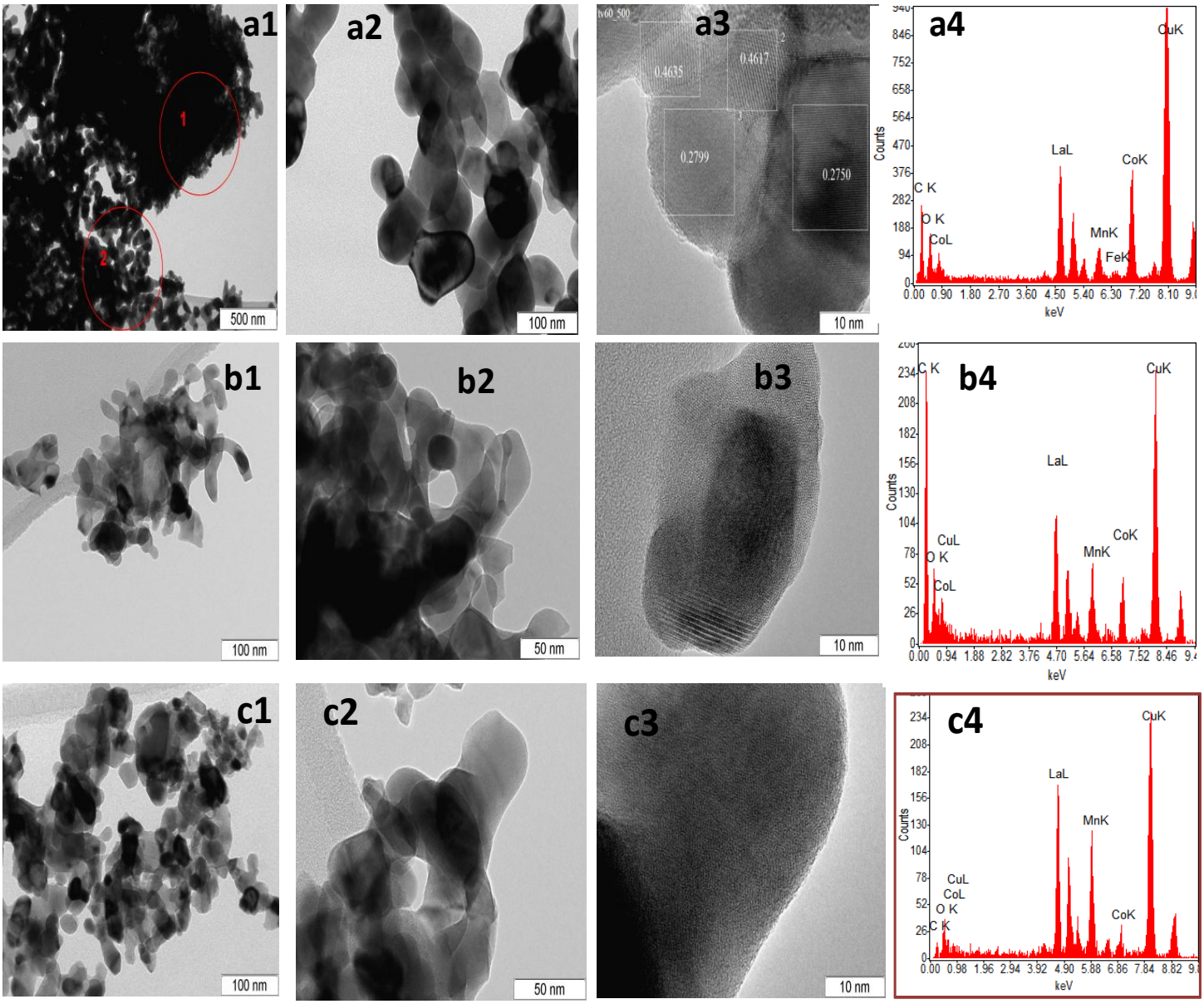

Figure 11.TEM images and EDX spectra for a1, a2, a3 and a4) $LaCo_{0.8}Mn_{0.2}O_{3,}$ b1, b2, b3 and b4)$LaCo_{0.5}Mn_{0.5}O_3$ and c1,c2,c3 and c4) $LaCo_{0.2}Mn_{0.8}O_3$

3.1.4. XPS Analysis of Simple and Hybrid Perovskites

Surface atomic ratios of simple perovskites (i.e. $LaCoO_3$ and $LaMnO_3$) obtained via current XPS measurements were found to be in good harmony with the formerly reported results in the literature [80]. Quantitative surface measurements via XPS are important to find out the relation between

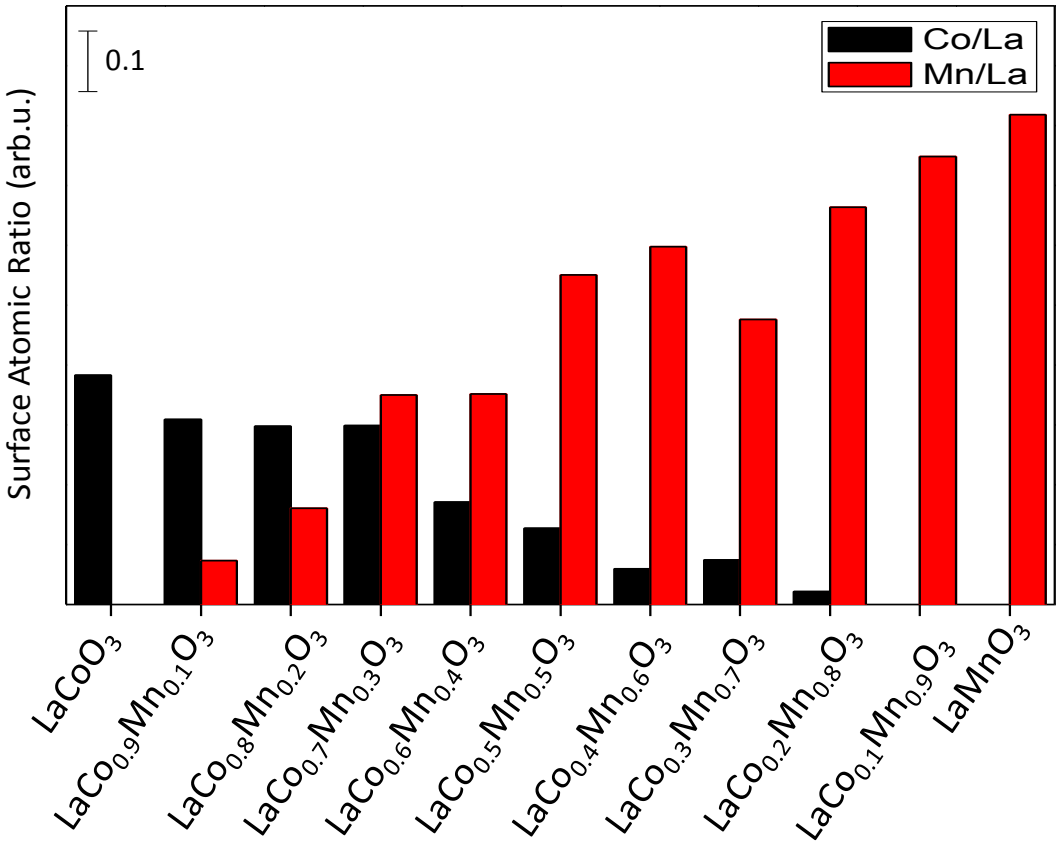

Figure 12. Quantitative analysis of surface atomic ratios via XPS for $LaCo_{0.x}Mn_{1-x}O_3$ type perovskites (x=0.0-1.0) calcined at 973 K.

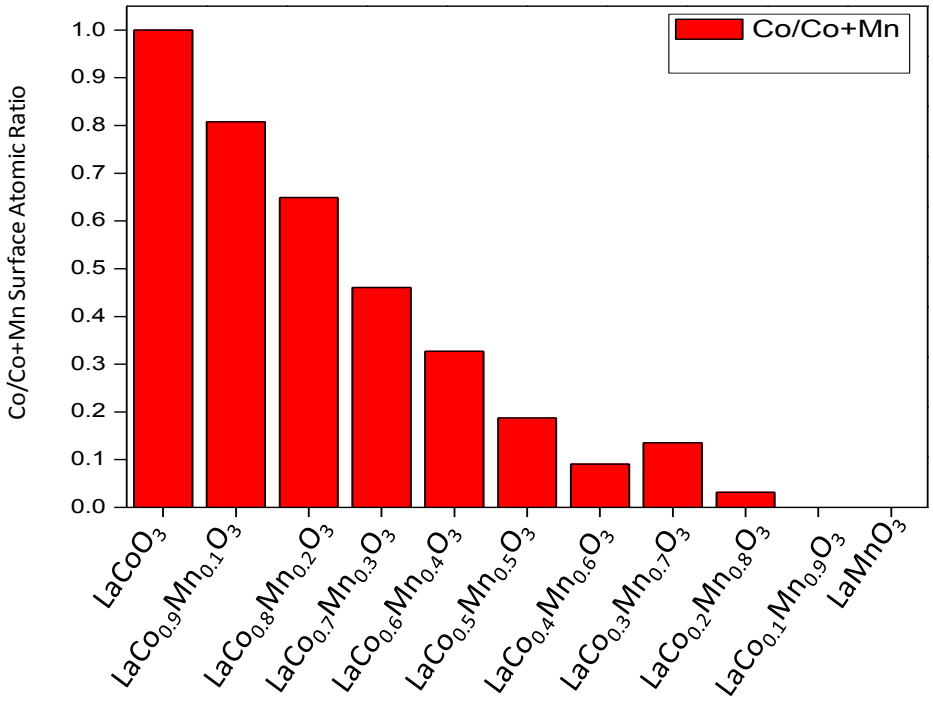

Figure 13. Relative Co surface atomic ratio with respect to the total Co and Mn surface atomic ratios (i.e. relative Co content present in all of the B sites comprised of Co and Mn species) for hybrid perovskites $LaCo_{0.x}Mn_{1-x}O_3$ (x=0.0-1.0).

NSC and NO_x oxidation or reduction activity. Figures 11 and 12, present the Mn/La, Co/La, Co/Co+Mn surface atomic ratios derived from current XPS measurements, using Pd3d, La3d, Mn2p, and Co3p XP spectra. These results clearly indicate that the Co/La surface atomic ratio decreases as a function of decreasing Co content in the hybrid perovskites, however the decrease in the Co/La surface atomic ratio does not have a linear dependence to the nominal bulk Co/La ratio corresponding to the metal precursor amounts used in the synthesis. It is important to note that for the entire synthesized hybrid and simple perovskite surfaces, surfaces were found to be enriched by La atoms (Table 5) this is in

agreement with a recent Density Functional Theory (DFT) study by W. F. Schneider et al. suggesting that $LaCoO_3$ perovskite surfaces are terminated by a La-O top layer which minimizes the surface Gibbs free energy of the lattice [85]–[87].

Table 5. Co/La and Mn/Lasurface atomic ratios (i.e. relative surface composition of B sites with respect to that of A sites) for $LaCo_{0.x}Mn_{1-x}O_3$ type hybrid perovskites (x=0.0-1.0) obtained via XPS

Sample Name	**Co/La**	**Mn/La**
$LaCoO_3$	0.38	0
$LaCo_{0.9}Mn_{0.1}O_3$	0.31	0.07
$LaCo_{0.8}Mn_{0.2}O_3$	0.30	0.16
$LaCo_{0.7}Mn_{0.3}O_3$	0.30	0.35
$LaCo_{0.6}Mn_{0.4}O_3$	0.17	0.35
$LaCo_{0.5}Mn_{0.5}O_3$	0.13	0.55
$LaCo_{0.4}Mn_{0.6}O_3$	0.06	0.60
$LaCo_{0.3}Mn_{0.7}O_3$	0.07	0.48
$LaCo_{0.2}Mn_{0.8}O_3$	0.02	0.66
$LaCo_{0.1}Mn_{0.9}O_3$	0	0.75
$LaMnO_3$	0	0.82

Table 6. Surface atomic ratios of all surface atoms (C,O,La,Co,Mn) of $LaCo_{0.x}Mn_{1-x}O_3$ type perovskites (x=0.0-1.0) obtained via XPS.

Sample Name	C	O	La	Co	Mn
$LaCoO_3$	33.3	50.8	11.5	4.4	0
$LaCo_{0.9}Mn_{0.1}O_3$	38.2	47.5	10.3	3.2	0.8
$LaCo_{0.8}Mn_{0.2}O_3$	29.9	52.3	12.2	3.6	2.0
$LaCo_{0.7}Mn_{0.3}O_3$	25.9	54.5	11.9	3.6	4.2
$LaCo_{0.6}Mn_{0.4}O_3$	29.8	49.8	13.4	2.3	4.7
$LaCo_{0.5}Mn_{0.5}O_3$	38.6	45.5	09.4	1.2	5.2
$LaCo_{0.4}Mn_{0.6}O_3$	37.6	45.2	10.4	0.6	6.2
$LaCo_{0.3}Mn_{0.7}O_3$	47.9	40.1	07.8	0.6	3.7
$LaCo_{0.2}Mn_{0.8}O_3$	42.9	41.6	09.2	0.2	6.1
$LaCo_{0.1}Mn_{0.9}O_3$	51.5	36.7	06.8	0.0	5.1
$LaMnO_3$	34.4	47.5	09.9	0.0	8.1

Co/Co+Mn surface atomic ratio points out a similar trend as shown in Figure 12 indicating that the surface coverage of Co decreases gradually as a function of decreasing nominal Co loading used in the synthesis procedure. Data given in Table 6 reveals that surface oxygen coverage is the highest for the $LaCo_{0.7}Mn_{0.3}O_3$ sample. Since XPS is a highly surface sensitive technique, current XPS data clearly indicate that the *"surface composition"* of the hybrid perovskites can be successfully fine-tuned by varying the synthetic protocol.

3.1.5. Ex-situ Infrared Analysis

Ex-situ infrared analyses were carried out for fresh hybrid perovskite catalysts after synthesis and calcination at 973 K without further treatment (Figures 13). While Figure 13a shows the 3D waterfall representation of the ex-situ FTIR spectra, Figure 13b presents a conventional 2D view of these spectra.

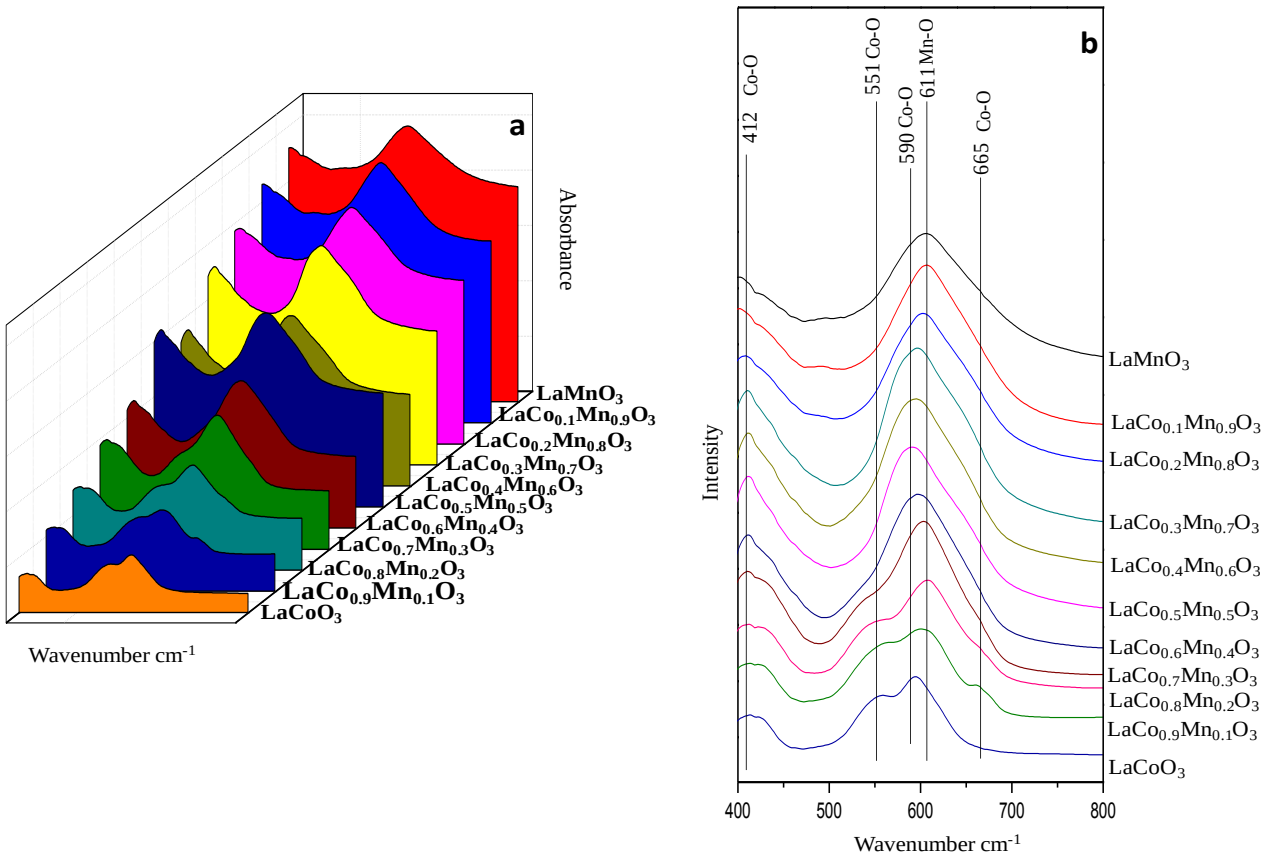

Figure 14. a) 3D-representation of the ex-situ FTIR spectra of the fresh $LaCo_{0.x}Mn_{1-x}O_3$ perovskites (x=0.0-1.0) after calcination at 973 K, **b**) 2D-representation of the ex-situ FTIR spectra of the fresh $LaCo_{0.x}Mn_{1-x}O_3$ perovskites (x=0.0-1.0) after calcination at 973 K.

Figures 13a and 13b show that there exists two characteristic vibrational stretchings for Co-O linkages, which are clearly visible for the spectrum corresponding to the $LaCoO_3$ sample which does not possess any Mn. This spectrum reveals two particular Co-O stretching of the CoO_6 octahedra located at 551 and 590 cm^{-1}. In addition, a weaker Co-O bending mode of the CoO_6 octahedra of the Co_3O_4 phase located at 665 cm^{-1} is also visible in Co-rich perovskites [88]–[90]. It is evident from Figures 13 and 14 that the 551 cm^{-1} feature which unambiguously originates only from Co-O species -and not from

Mn-O species- gradually attenuates with increasing Mn content in the hybrid perovskites; indicating that the *"bulkcomposition"* of the perovskites can be fine-tuned successfully by varying the nominal Co and Mn precursor loadings in the synthetic protocol.

3.1.6. NO_x Adsorption on Fresh and Reduced Perovskites

Figure 15 shows in-situ FTIR spectra corresponding to NO_2 adsorption on a representative *fresh* hybrid-perovskite which was initially activated with 0.5 Torr NO_2 and annealed to 973 K, as described earlier. Each of the successive spectra given in Figure 15 involves an additional dose for 1 Torr NO_2 for duration of 1 min at 323 K, followed by evacuation and spectrum acquisition. The last (i.e. the topmost) spectrum corresponds to the saturation of the surface with excess NO_2 (5 Torr, 10 min) at 323 K.

As can be seen in Figure 14, NO_2 and surface interaction leads to the evolution of various IR bands located within 1000-1800 cm^{-1} which are associated with nitrate (NO_3^-) and nitrite (NO_2^-)species [91]–[96]. IR bands at 1639 and 1006 cm^{-1}can be attributed to the symmetric and asymmetric modes of bridging nitrates; respectively [91].

In Figure 15, bidentate nitrates can be observed at 1575 and 1257 cm^{-1} [92], [93]. IR bands of nitrito species can also be detected in Figure 14 at 840-820 cm^{-1} (ν_{ONO}, bending), 1365-1075 cm^{-1} (ν_{N-O}) and1485-1400 cm^{-1} ($\nu_{N=O}$). Thus, the

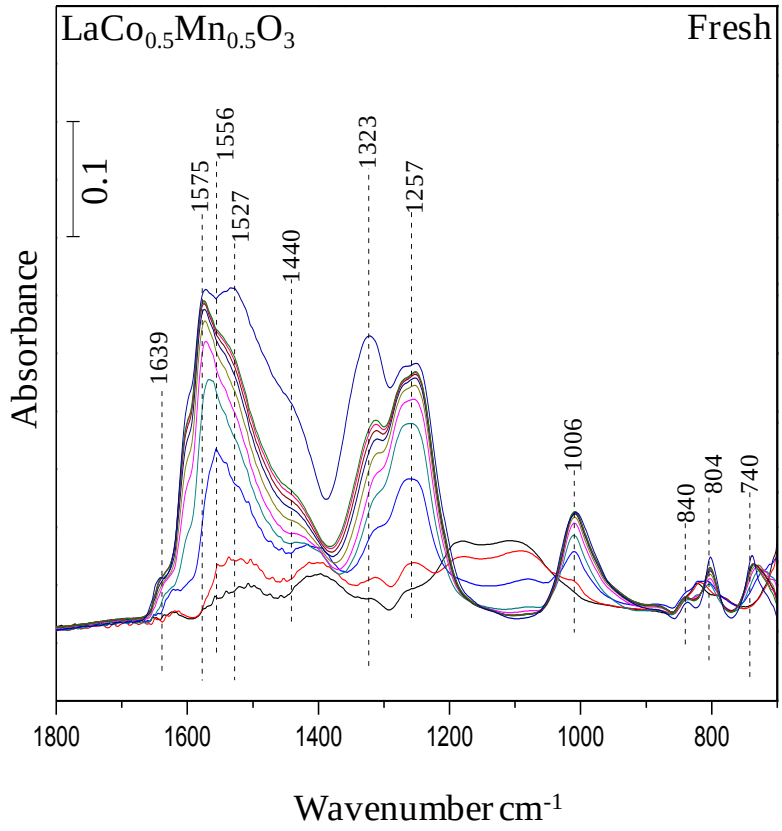

Figure 15.In-situ FTIR specta corresponding to the stepwise NO_2 adsorption and saturation of fresh $LaCo_{0.5}Mn_{0.5}O_3$ catalyst at 323 K.

signals at 1440, 1323 and 840 cm^{-1} can be ascribed to nitrito species (i.e. nitrites).IR signals in Figure 14 at 1174 and 1090 cm^{-1}belong to nitrite vibrational modes vanishing at high exposures of NO_2 due to the oxidation of nitrites into nitrates. Adsorption process can be explained by following reaction mechanism:

$2NO_2$ (adsorbed) + O^{2-} (surface)→NO_3^- (adsorbed) + NO_2^- (adsorbed) [80] *(6)*

Stepwise NO_x adsorption was also performed on perovskites other than $LaCo_{0.5}Mn_{0.5}O_3$. Figures 15-17 present similar experiments performed on all of the

hybrid perovskites in addition to simple perovskites (i.e. $LaCoO_3$ and $LaMnO_3$).In-situ FTIR results given in Figures 15-17 suggest that the adsorption geometries of nitrate and nitrito species on the catalyst surfaces are quite alike. This is in agreement with the previously discussed current XPS results, which indicated that the topmost perovskite surfaces are enriched with La and thus, NO_x adsorption bands on the synthesized perovskite surfaces closely resemble that of La_2O_3 [80]. In other words, it is likely that the B-sites are likely to be located -at least to a certain extent-below the La-O surface termination. Hence, NO_x adsorption geometry is not altered significantly as a function of the B-site composition.

Perovskites have a quite dynamic electronic structure associated with their oxygen vacancies as well as reversible redox properties associated with their A and B-site cations. Oxidation states of A and B site cations and oxygen mobility are crucial aspects associated with cyclic catalytic redox reactions such as NSR catalysis. In order to understand such properties mentioned above, interaction of NO_2 with perovskite surfaces after reduction with H_2 was also studied. Reduced catalysts were prepared after exposing as-prepared catalysts which are initially calcined at 973 K to 5 Torr H_2 for 10 min at 623 K. Then these surfaces were saturated with 5 Torr NO_2.

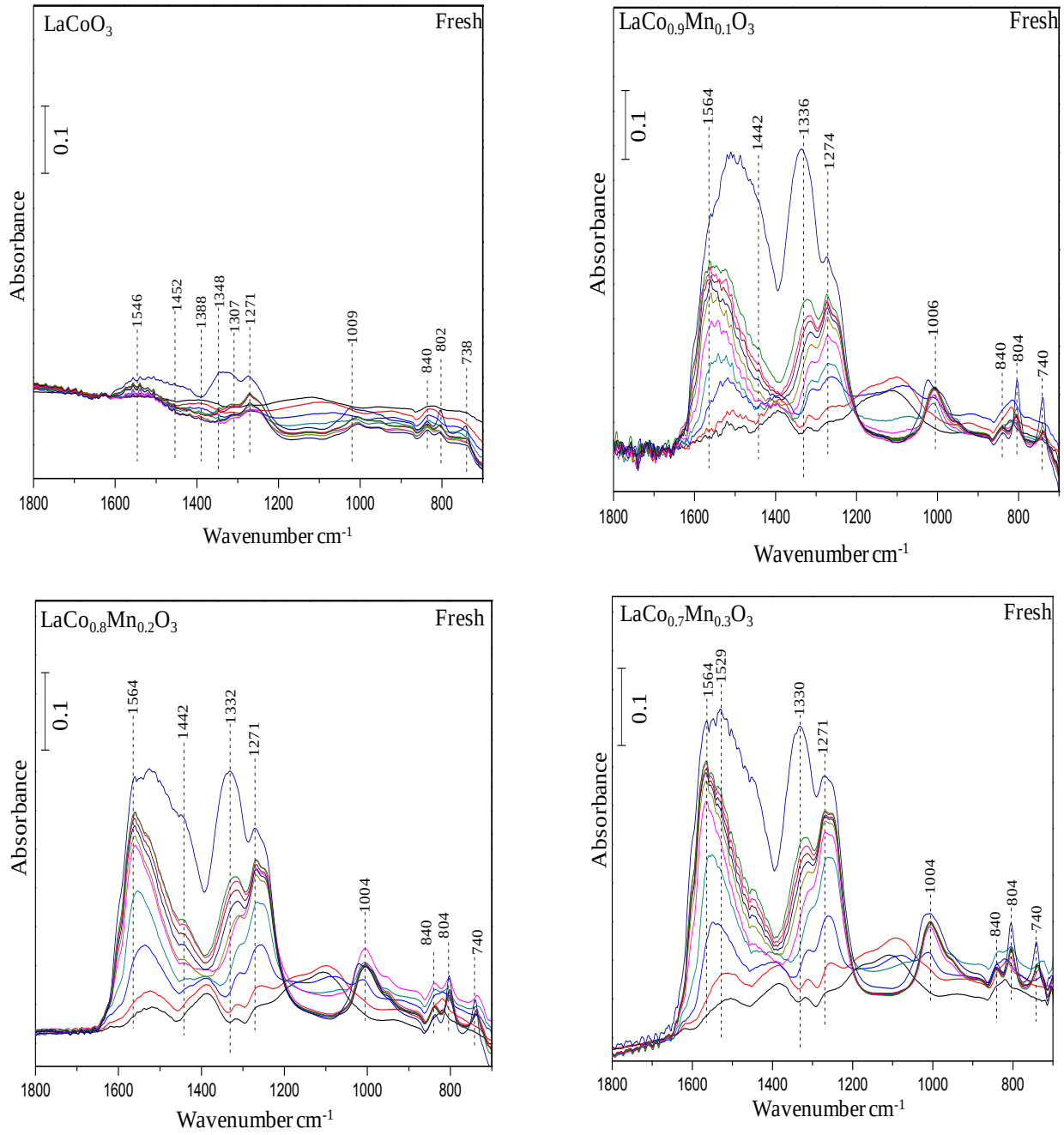

Figure 16. Stepwise NO_2 adsorption on $LaCo_xMn_{1-x}O_3$ hybrid perovskites where $(0 \leq x \leq 0.3)$ at 323 K.

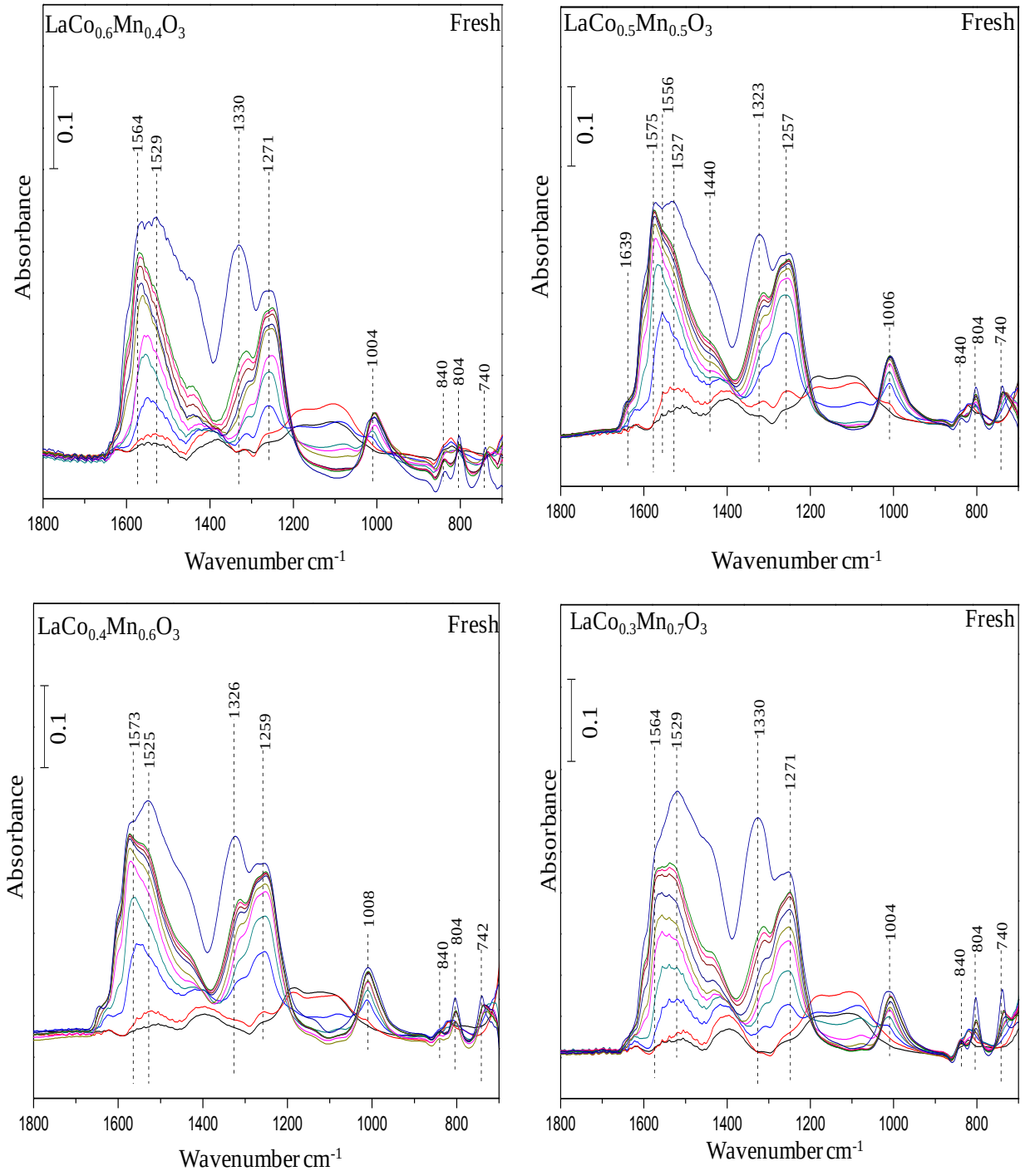

Figure 17. Stepwise NO_2 adsorption on $LaCo_xMn_{1-x}O_3$ hybrid perovskites where $(0.4 \leq x \leq 0.7)$ at 323 K.

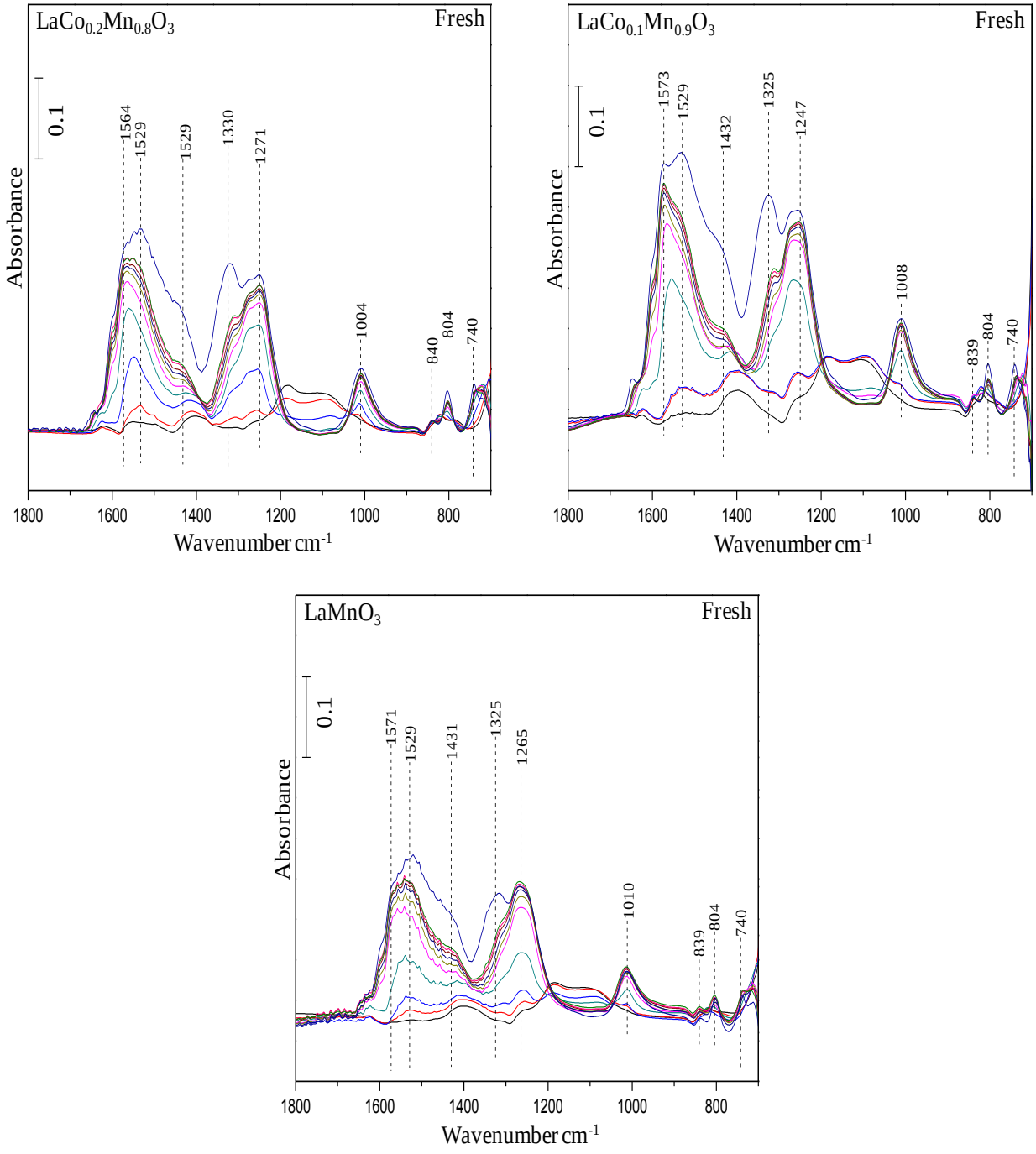

Figure 18. Stepwise NO_x adsorption of $LaCo_xMn_{1-x}O_3$ type perovskites

(0.8≤x≤1.0) at 323 K.

In Figure 18, blue in-situ FTIR spectrum corresponds to the NO_2 saturation of the fresh $LaCo_{0.5}Mn_{0.5}O_3$ catalyst (i.e. without reduction) whereas green spectrum corresponds to a similar experiment on the reduced catalysts. Comparison of the fresh and reduced catalysts readily reveals that the reduced catalyst has a much

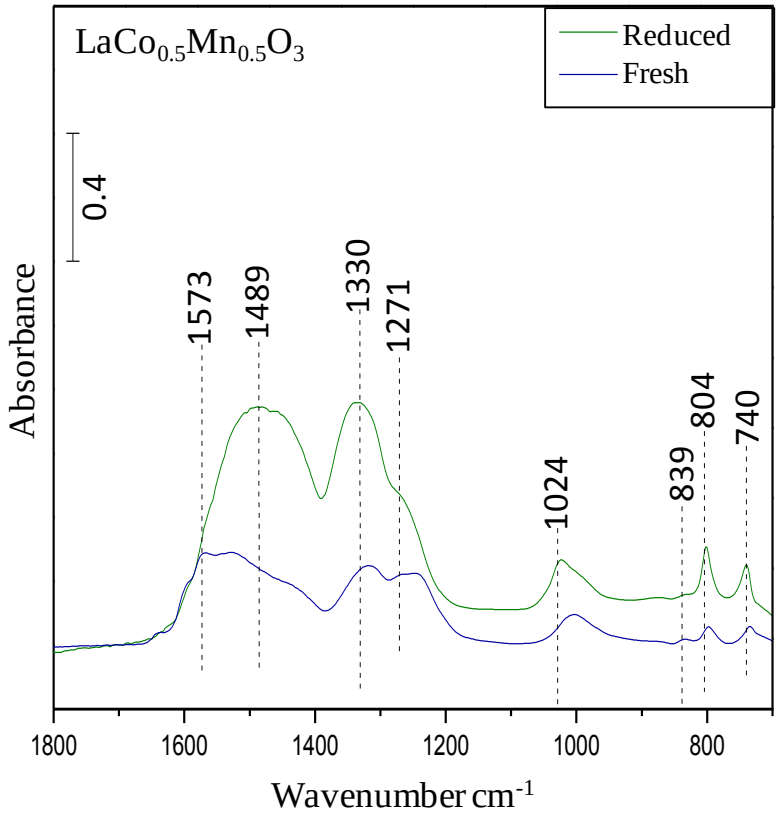

Figure 19. NO_x adsorption (5 Torr NO_2) spectra of reduced and fresh $LaCo_{0.5}Mn_{0.5}O_3$ at 323 K

higher NO_2 storage capacity. It is likely that reduction of perovskites creates oxygen vacancy sites which modify the oxygen mobility on the surface[88], [89]

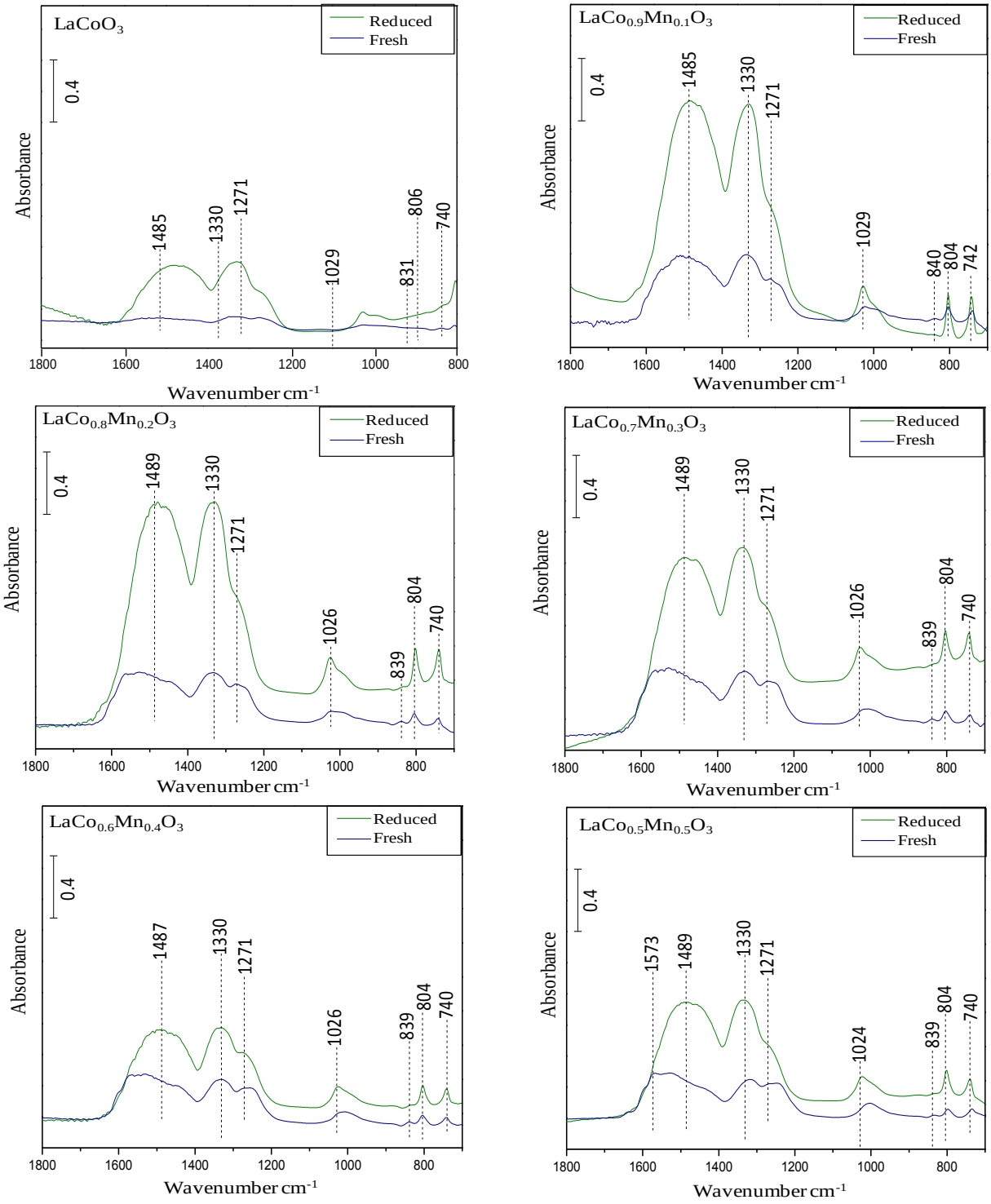

Figure 20. In-situ FTIR spectra for NO_2 adsorption on reduced and fresh

$LaCo_xMn_{1-x}O_3(0\leq x\leq 0.5)$at 323 K

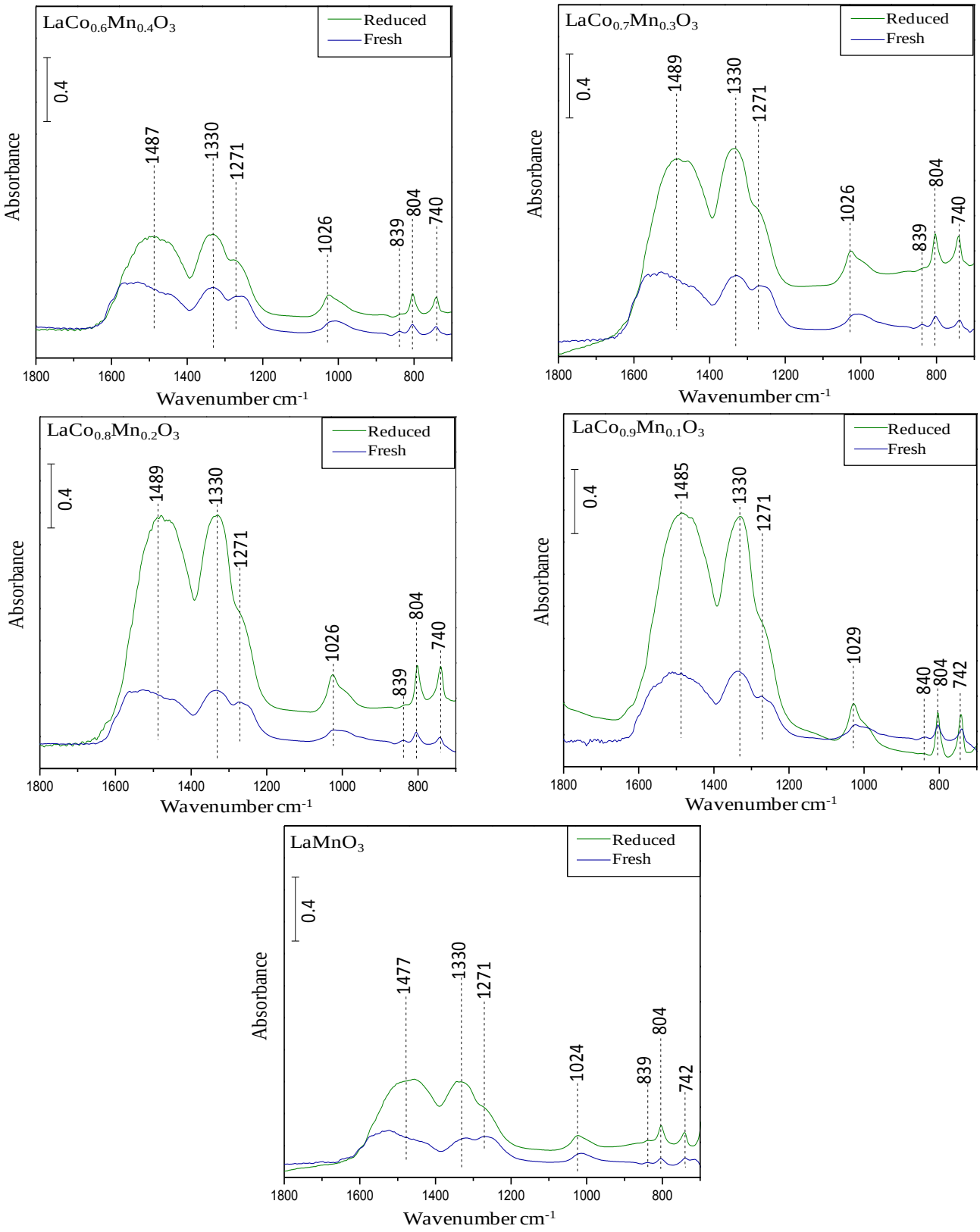

Figure 21. NO_x adsorption spectra of reduced and fresh $LaCo_xMn_{1-x}O_3$ ($0.6 \leq x \leq 1$) at 323 K.

generates new anchoring defect sites that can facilitate NO_2 adsorption, N-O bond activation and oxidation which in turn, results in enhanced storage of NO_2 on the surface. Therefore it can be concluded that NO_x adsorption capacity of perovskites is improved by the reduction process. Similar in-situ FTIR experiments were also performed for other hybrid-perovskite catalysts which are presented in Figures 19 and 20.

3.1.7. NO_x TPD of Fresh and Reduced Perovskites

NO_2 saturated perovskites were investigated by TPD experiments. NO_x release from the synthesized catalyst surface was monitored by QMS to identify the link between NO_x storage capacity and B-site substitution. Before the first TPD experiment, multiple 1.0 Torr NO_2 exposures were introduced on the samples at 323 K as described for Figures 15, 16 and 17; followed by complete saturation using a 5 Torr NO_2 exposure for 10 min at 323 K. After NO_2 saturation, TPD experiments were performed. In the successive TPD experiment, NO_x uptake on the reduced catalyst was investigated after an exposure of 5 Torr H_2 at 623 K without changing the sample that already exists in the IR-TPD system. Once the sample was reduced with H_2, reactor was evacuated and 5 Torr NO_2 was dosed over the sample and the "reduced" catalyst was saturated with NO_x. Relevant desorption channels for the NO_2-TPD experiments over fresh and reduced catalysts are plotted in Figures 21-23.

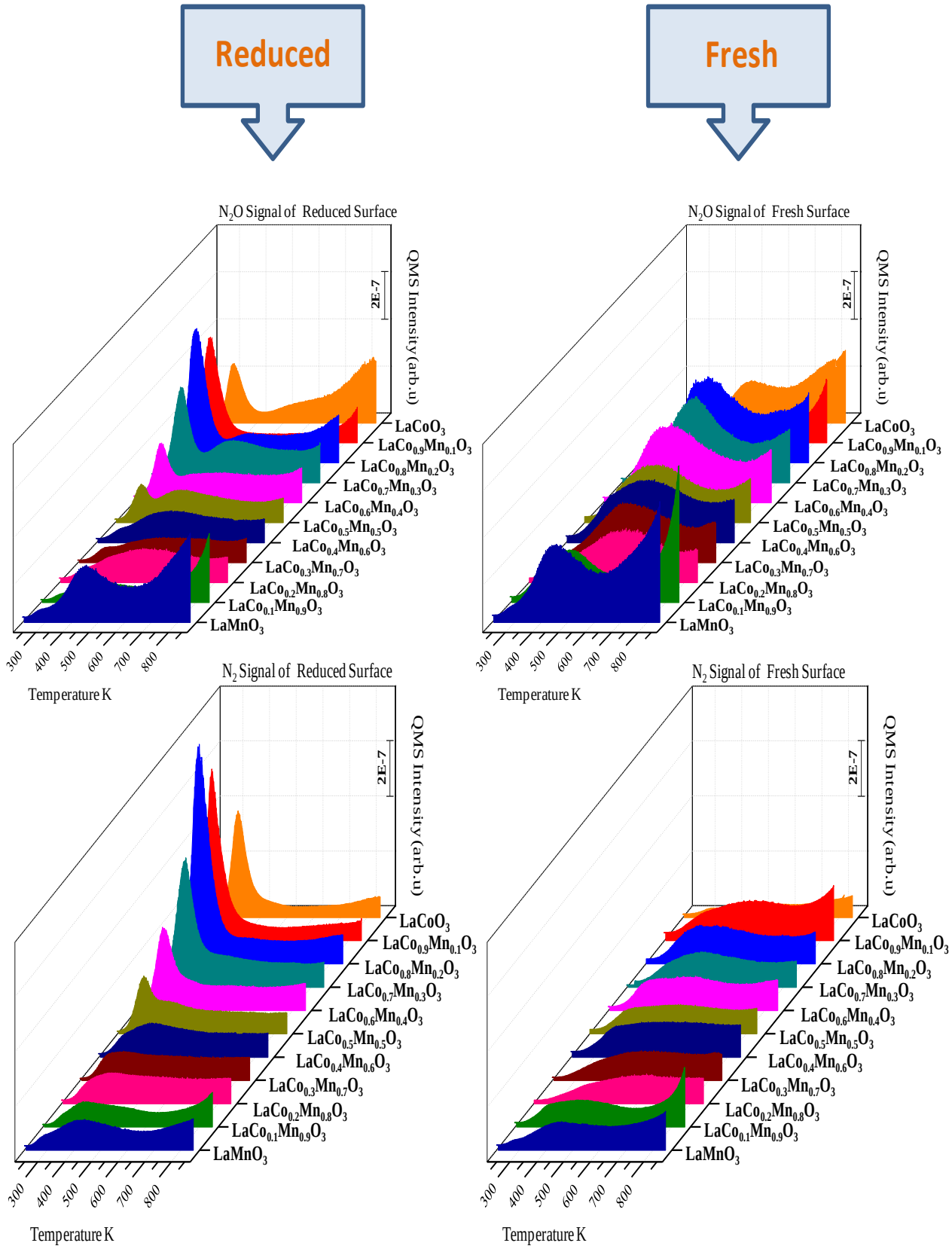

Figure 22. N_2O and N_2 TPD signals of pre-reduced and fresh $LaCo_xMn_{1-x}O_3$ ($0 \leq x \leq 1$) catalysts obtained after saturation with NO_2 at 323 K.

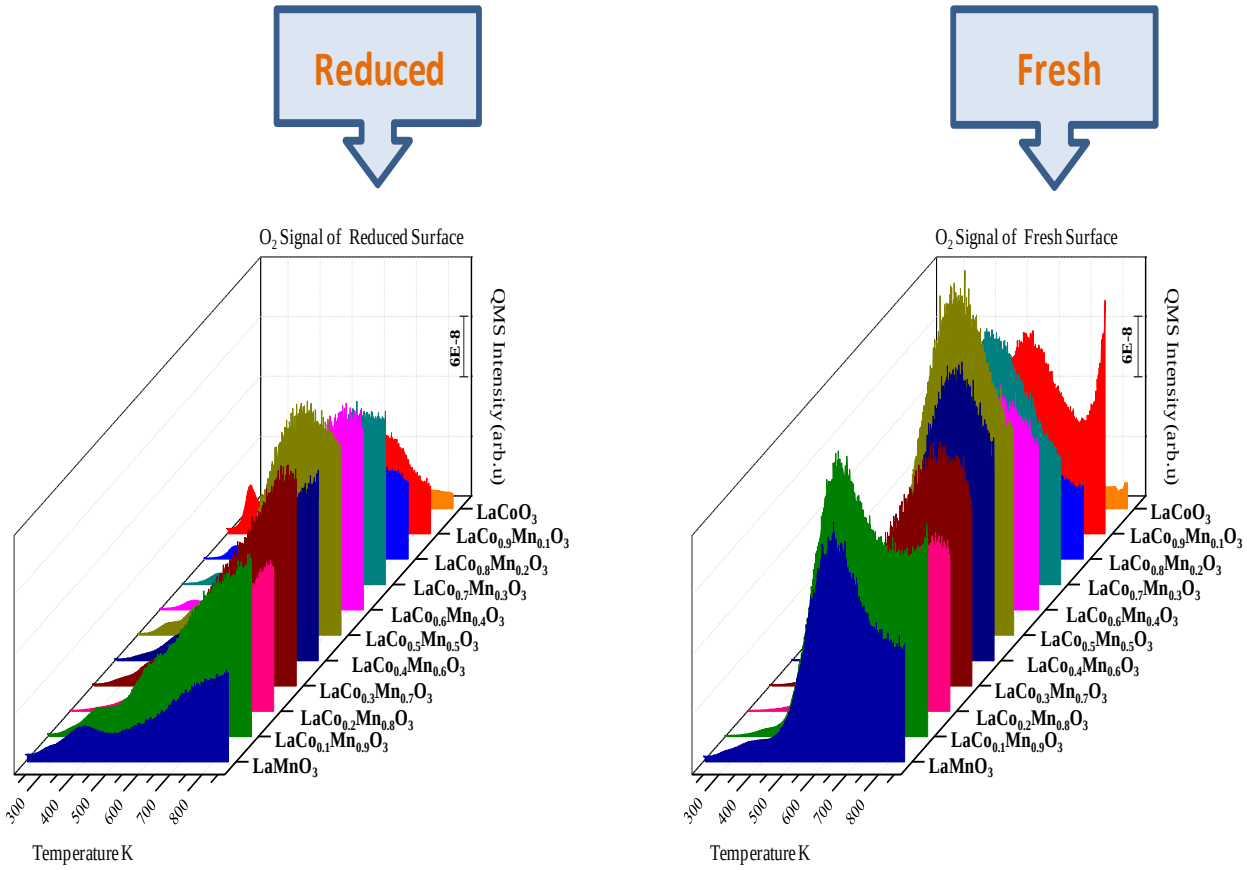

Figure 23. O_2 TPD signals of pre-reduced and fresh $LaCo_xMn_{1-x}O_3$ ($0 \leq x \leq 1$) catalysts obtained after saturation with NO_2 at 323 K.

Furthermore, quantitative analysis of the NO_x TPD experiments were also performed by integrating the areas under the particular desorption curves in order to compute the total NO_x storage capacities of hybrid and simple perovskites. For the quantitative TPD analysis, mass spectrometer fragmentation factors obtained from NIST database [97] were employed in order to normalize the integrated area values for each desorption channel. Calculations of the total NO_x storage values were performed by calculating the corrected relative amounts of each NO_x species using the following equations, where "I_x" represents the integrated raw area of a particular desorption channel "x":

$$\sum NO_2 = I_{46} \times 3.98 \quad (8)$$

$$\sum N_2O = I_{44} \times 1.325 \quad (9)$$

$$\sum NO = [I_{30} - I_{44} \times 0.31 - I_{46} \times 2.72] \times 1.08 \quad (10)$$

$$\sum N_{2=} [I_{28} - I_{44} \times 0.11] \times 1.13 \quad (11)$$

$$\text{Total } NO_x \text{ Storage} = \sum NO_2 + 2\sum N_2O + \sum NO + 2\sum N_2 \quad (12)$$

"$\sum x$" symbol used above represents the corrected number of molecules "x" desorbing from the catalyst surface which contributes to the total NO_x storage. It should be noted that some of the NO_x species are comprised of 2N atoms per molecule such as N_2O and N_2. Hence their corrected integrated desorption signals should be multiplied by two. Total NO_x storage capacities of all of the investigated perovskites are given in Table 7 and Figure 24. Comparison of the simple perovskites suggests that fresh $LaMnO_3$ has a higher NSC than that of fresh $LaCoO_3$.This is consistent with one of our earlier reports where this behavior was attributed mostly to the significantly higher specific surface area of the $LaMnO_3$ catalyst [80]. On the other hand, comparison of the NSC values of all perovskite catalysts including simple and hybrid perovskites indicates that $LaCo_{0.8}Mn_{0.2}O_3$ and $LaCo_{0.7}Mn_{0.3}O_3$ catalysts have relative higher NSC in their fresh as well as reduced forms. Table 7 reveals a volcano plot for the variation of the NSC as a function of catalyst composition where the NSC values seem to reach optimal values for $LaCo_{0.8}Mn_{0.2}O_3$ and $LaCo_{0.7}Mn_{0.3}O_3$. It is important to note that this enhancement in NO_x oxidation and storage capacity is not merely due to differences in specific surface area; as these two superior catalysts have

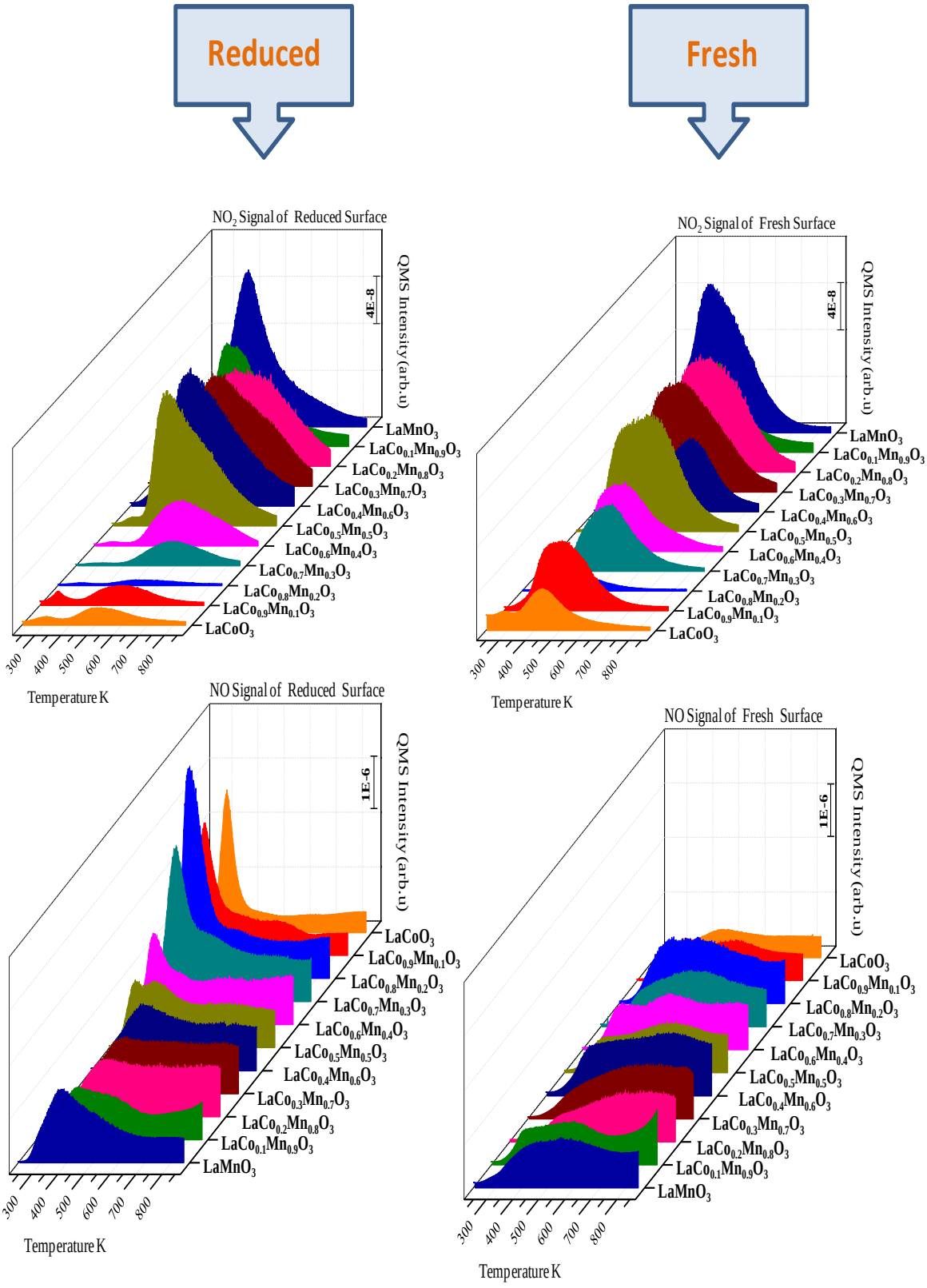

Figure 24.NO and NO_2 TPD signals of pre-reduced and fresh $LaCo_xMn_{1-x}O_3$ ($0 \leq x \leq 1$) catalysts obtained after saturation with NO_2 at 323 K.

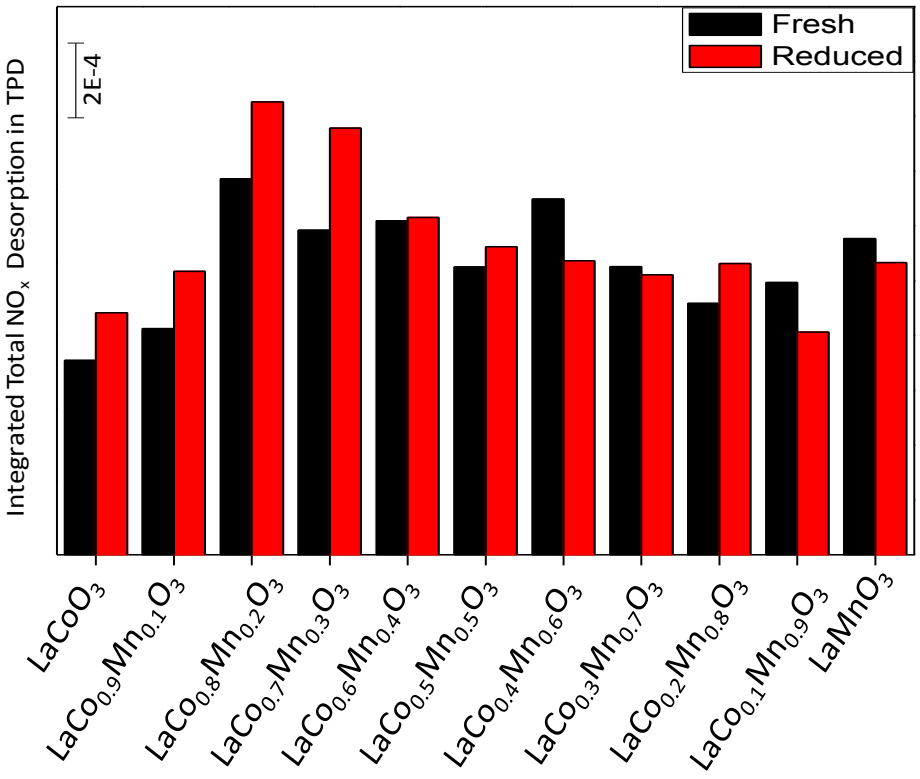

Figure 25. Total relative NO_x storage capacities of reduced and fresh catalysts in the form of $LaCo_xMn_{1-x}O_3$ ($0 \leq x \leq 1$) obtained after saturation with NO_2 at 323 K..

lower SSA than many of the other synthesized catalysts (Table 4, Figure 9) Optimal NSC values for $LaCo_{0.8}Mn_{0.2}O_3$ and $LaCo_{0.7}Mn_{0.3}O_3$ can be linked to their surface compositions which were analyzed in detail in the current XPS investigations (Table 6). Current XPS results show that $LaCo_{0.8}Mn_{0.2}O_3$ and $LaCo_{0.7}Mn_{0.3}O_3$ have the highest surface atomic oxygen, which may facilitate the oxidation of NO, NO_2 and nitrite species and their efficient storage in the form of nitrates.

It is important to mention that N_2O and N_2 desorption signals of pre-reduced $LaCo_{0.8}Mn_{0.2}O_3$ and $LaCo_{0.7}Mn_{0.3}O_3$ catalysts are also particularly unique. Figure 21 shows that there exists very intense N_2 and N_2O release at 325-375K for these two particular catalysts. Since formation/desorption of N_2 and N_2O implies

direct N-O bond activation in the initial NO_2 adsorbate, it is clear that $LaCo_{0.8}Mn_{0.2}O_3$ and $LaCo_{0.7}Mn_{0.3}O_3$ catalysts can readily perform NO_x reduction, possibly thorough the involvement of Co/Co^{2+} redox species [79], [80].

It can be seen in the TPD data given in Figure 23 that during the nitrate decomposition, O_2(g) evolution does not always accompany NO, NO_2 and N_2O desorption. In other words, it is observed that some of the oxygen that is created due to nitrate decomposition is consumed by the lattice, where the generated atomic oxygen titrates the oxygen vacancies on the surface and/or in the bulk rather than recombinatively desorbing in the form of molecular oxygen [98]. In addition to this NO release In Figure 23 on fresh perovskite is significantly higher than total NO_2 release however there is two possible pathway for nitrate decomposition: first nitrate can decomposes as NO_2+1/O_2 and second is $NO+O_2$. Released NO_2 can decomposed as $NO+1/2O_2$ based on the fragmentation pattern with a ratio $NO/ NO_2=2.72$. Oxygen evolution from NO_2 decomposition also alters the released amount of oxygen. In addition to that, O_2 desorption levels of fresh catalysts are drastically higher than the reduced ones suggesting that reduction process significantly depletes the surface oxygen species and possibly some of the oxygen species in the bulk perovskite lattice.

Table 7. Integrated TPD desorption signals and total relative NO_x storage values for reduced perovskite catalysts $LaCo_xMn_{1-x}O_3$ ($0 \leq x \leq 1$).

Sample Name	I_{46} (NO_2)	I_{30}(NO)	I_{44} (N_2O)	I_{28} (N_2)	Total NO_x
$LaCoO_3$	2,93E-5	3,35E-4	7,48E-5	5,08E-5	6,62E-4
$LaCo_{0.9}Mn_{0.1}O_3$	2,20E-5	4,45E-4	5,74E-5	6,80E-5	7,76E-4
$LaCo_{0.8}Mn_{0.2}O_3$	2,75E-5	7,06E-4	1,04E-4	1,03E-4	1,24E-3
$LaCo_{0.7}Mn_{0.3}O_3$	3,07E-5	6,83E-4	1,02E-4	8,29E-5	1,17E-3
$LaCo_{0.6}Mn_{0.4}O_3$	3,33E-5	5,36E-4	7,68E-5	6,69E-5	9,23E-4
$LaCo_{0.5}Mn_{0.5}O_3$	2,83E-5	5,09E-4	6,45E-5	5,79E-5	8,43E-4
$LaCo_{0.4}Mn_{0.6}O_3$	1,11E-5	5,06E-4	5,97E-5	5,49E-5	8,05E-4
$LaCo_{0.3}Mn_{0.7}O_3$	5,89E-6	5,00E-4	5,15E-5	5,03E-5	7,66E-4
$LaCo_{0.2}Mn_{0.8}O_3$	1,80E-6	5,01E-4	6,38E-5	5,43E-5	7,97E-4
$LaCo_{0.1}Mn_{0.9}O_3$	5,74E-6	3,73E-4	5,19E-5	4,13E-5	6,09E-4
$LaMnO_3$	5,01E-6	4,29E-4	1,06E-4	4,96E-5	7,99E-4

Table 8. Integrated TPD desorption signals and total relative NO_x storage values for fresh perovskite catalysts $LaCo_xMn_{1-x}O_3$ ($0 \leq x \leq 1$).

Sample Name	I_{46} (NO_2)	I_{30}(NO)	I_{44} (N_2O)	I_{28} (N_2)	Total NO_x
$LaCoO_3$	3,25E-5	2,34E-4	8,73E-5	2,87E-5	5,32E-4
$LaCo_{0.9}Mn_{0.1}O_3$	1,75E-5	3,02E-4	5,16E-5	7,38E-5	6,19E-4
$LaCo_{0.8}Mn_{0.2}O_3$	3,00E-5	5,31E-4	1,36E-4	6,29E-5	1,03E-3
$LaCo_{0.7}Mn_{0.3}O_3$	2,94E-5	4,45E-4	1,22E-4	5,52E-5	8,88E-4
$LaCo_{0.6}Mn_{0.4}O_3$	1,67E-5	4,66E-4	1,26E-4	5,87E-5	9,14E-4
$LaCo_{0.5}Mn_{0.5}O_3$	2,91E-5	4,04E-4	9,91E-5	5,14E-5	7,87E-4
$LaCo_{0.4}Mn_{0.6}O_3$	1,53E-5	5,35E-4	1,13E-4	6,45E-5	9,74E-4
$LaCo_{0.3}Mn_{0.7}O_3$	1,38E-5	4,28E-4	9,69E-5	4,92E-5	7,88E-4
$LaCo_{0.2}Mn_{0.8}O_3$	3,42E-6	3,71E-4	8,64E-5	4,64E-5	6,88E-4
$LaCo_{0.1}Mn_{0.9}O_3$	1,51E-5	3,74E-4	1,02E-4	5,10E-5	7,45E-4
$LaMnO_3$	9,31E-6	4,03E-4	1,46E-4	5,21E-5	8,65E-4

Figure 23 compares NO and NO_2 desorption channels for fresh and pre-reduced perovskites. Interestingly, NO_2 release is not affected significantly by the reduction process. It can be argued that NO_2 desorption signal mostly originates from nitrate species which are associated with rather stoichiometric/fully oxidized

surface/bulk perovskite domains which do not possess a high concentration of oxygen vacancies. In stark contrast, Figure 23 clearly shows that this is not the case for the NO desorption signal where NO release is remarkably higher for the reduced perovskites. Furthermore, this marked increase in the NO_x desorption in the form of NO appears at relatively lower temperatures than the usual NO_x release from fresh perovskites. It is likely that this accentuated NO release is due to nitrates which are bound to oxygen vacancies generated on the reduced perovskite surfaces which can readily decompose at low temperatures by leaving atomic oxygen species behind. These atomic oxygen species may cure the oxygen vacancies and titrate the defects on the surface as well as in the bulk. Tables 7-8 and Figure 24 present a numerical comparison of the total NO_x storage capacities of all of the fresh and synthesized perovskites investigated in the current study by calculating the corrected number of desorbing molecules using mass spectroscopic fragmentation factors. As discussed earlier, these results clearly emphasize the superior NSC of fresh and reduced forms of $LaCo_{0.8}Mn_{0.2}O_3$ and $LaCo_{0.7}Mn_{0.3}O_3$ catalysts compared to all of the other currently synthesized perovskites.

3.1.8. SO_x Adsorption and Reduction via H_2

In this part of the current study, SO_x interactions with perovskite surfaces were investigated by using in-situ FTIR technique. Before SO_x experiments, catalysts were heated to 973 K and then were exposed to 2 Torr SO_x gas mixture (SO_2:O_2= 1:10). Samples were heated to various temperatures within 373-673 K in the presence of SO_x for 10 min. Next, poisoned samples were exposed to 0.5

Torr H_2 after evacuation of SO_x and each sample was heated at 373,773,873 and 973 K for 10 min in the presence of H_2 so as to remove SO_x species adsorbed on the surfaces. Figure 25, shows a typical set of in-situ FTIR spectra for SO_x uptake and reduction experiments performed over $LaCo0._5Mn_{0.5}O_3$.Similar experiments were also performed over all of the investigated hybrid perovskites which are illustrated in Figures 26 and 27. In Figure 25, upper set of spectra correspond to

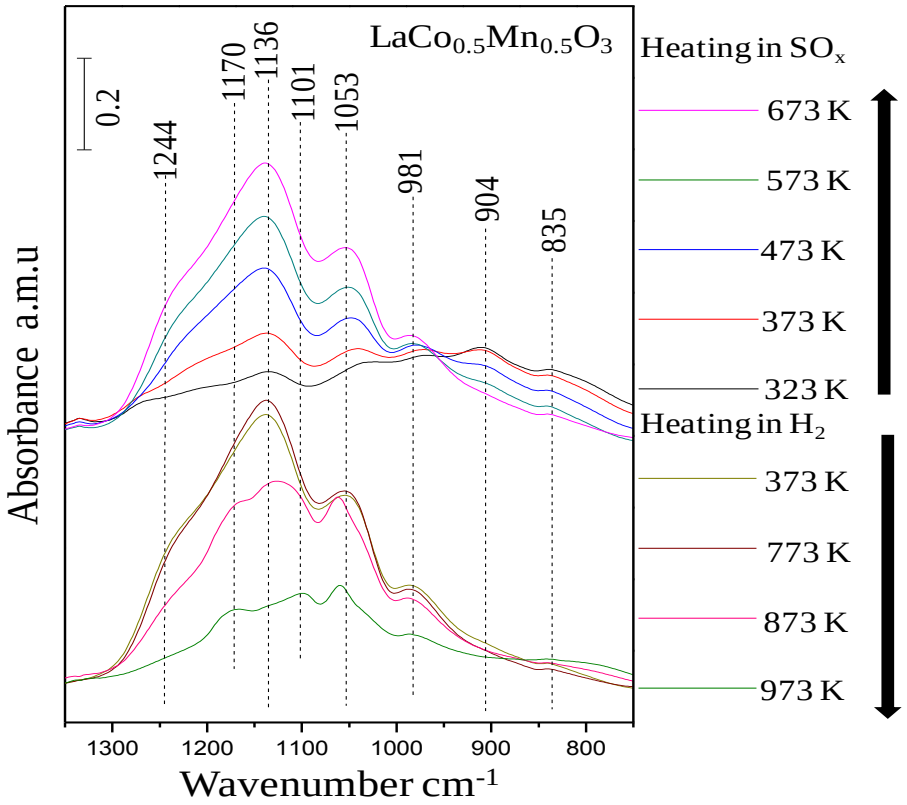

Figure 26. In-situ FTIR spectra for SO_x adsorption and subsequent reduction with hydrogen for $LaCo_{0.5}Mn_{0.5}O_3$

the SO_x uptake in the presence of the SO_x gas mixture , while the set of spectra at the bottom corresponds to the reduction of the sulfur saturated surfaces with hydrogen at various temperatures.IR bands at 1170,1136,1101 and 1053 cm^{-1} can be assigned to bulk sulfate species [71], [99]–[101] while peaks around 1244

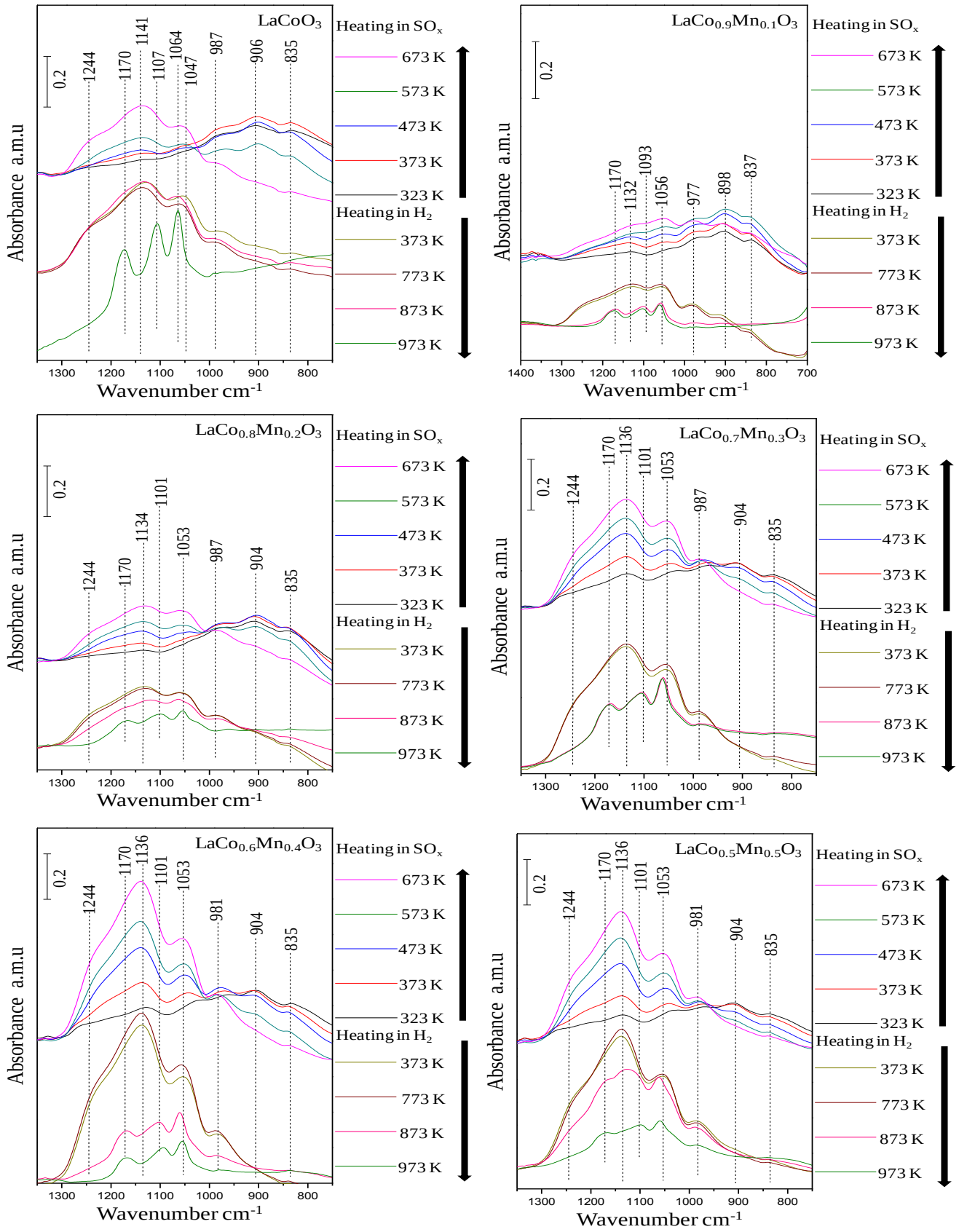

Figure 27. In-situ FTIR spectra for SO_x adsorption and subsequent reduction with hydrogen for $LaCo_xMn_{1-x}O_3$ ($0.0 \leq x \leq 0.5$)

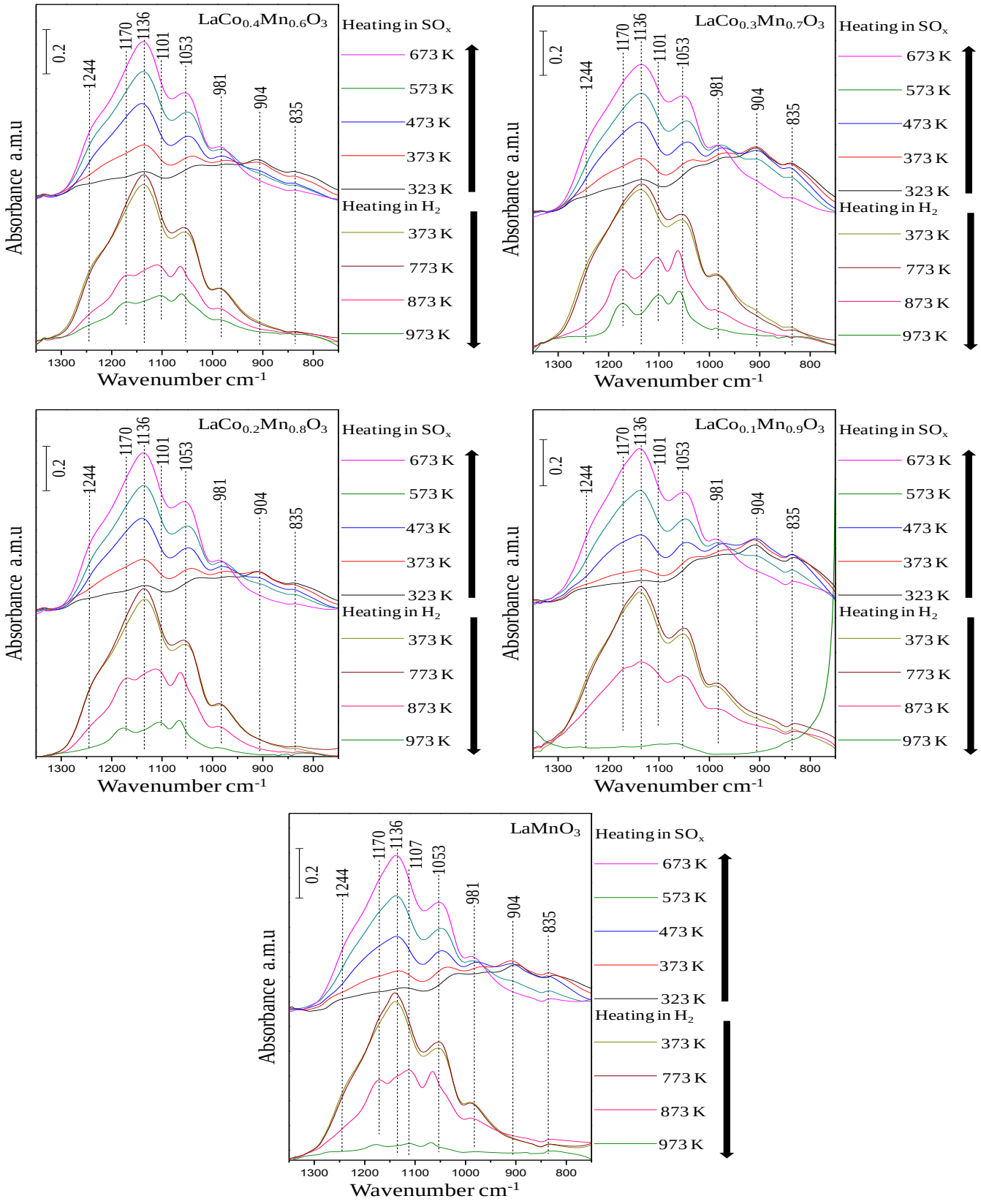

Figure 28 . In-situ FTIR spectra for SO_x adsorption and subsequent reduction with hydrogen for $LaCo_xMn_{1-x}O_3$ ($0.6 \leq x \leq 1.0$)

and 981 cm^{-1} can be attributed to bidentate surface sulfates [99], [101]. Furthermore, the IR signal at 904 cm^{-1} can be associated with sulfite species [101]. The weak shoulder located around 835 cm^{-1} can be due to residual carbonate species originating from the citrate precursor used in the synthesis [100]. Comparing the upper set of spectra in Figures 26 and 27, it can be seen that the sulfur uptake profiles of the hybrid perovskites depend strongly on the nature of the B-site cations. Due to their higher specific surface areas, Mn-rich perovskites seem to store significantly higher amount of sulfates and sulfites as compared to Co-rich perovskites. On the other hand, comparing the reduction behavior of the sulfur poisoned samples (i.e. lower set of spectra given in Figures 26 and 27) in hydrogen suggests that, while Mn-rich perovskites can eliminate sulfur with a relatively higher efficiency, Co-rich perovskites lead to irreversible poisoning generating strongly bound and bulk-like sulfates with sharp vibrational features. Thus it can be argued that by fine-tuning the B-site cations and catalyst composition, sulfur tolerance of the hybrid perovskites can also be changed in a controlled manner.

In addition, there exists an isosbestic point around at 958 cm^{-1} indicating that with the increasing temperature in the presence of the SO_x gas mixture, IR intensities of sulfite and carbonate species (at 904 and 835 cm^{-1}; respectively)gradual diminish while sulfate features gain intensity. This observation suggests the substitution/conversion of sulfites and carbonates with/to sulfates.

3.1.9. SO_x and NO_x co-Adsorption on Perovskites

SO_x and NO_x co-adsorption experiments were also performed on hybrid perovskites in order to investigate the competition between NO_x with SO_x species for surface adsorption sites. In these set of experiments, perovskite samples were initially heated to 973 K and then the surfaces were saturated with 5 Torr NO_2. After NO_2 saturation, perovskite samples were heated up to 973 K once again in order to remove the NO_x species on the surface. Finally, SO_x/NO_x mixture with 1/5 partial pressure ratio (SO_2:O_2:NO_2= 1:10:55) was prepared and dosed over the

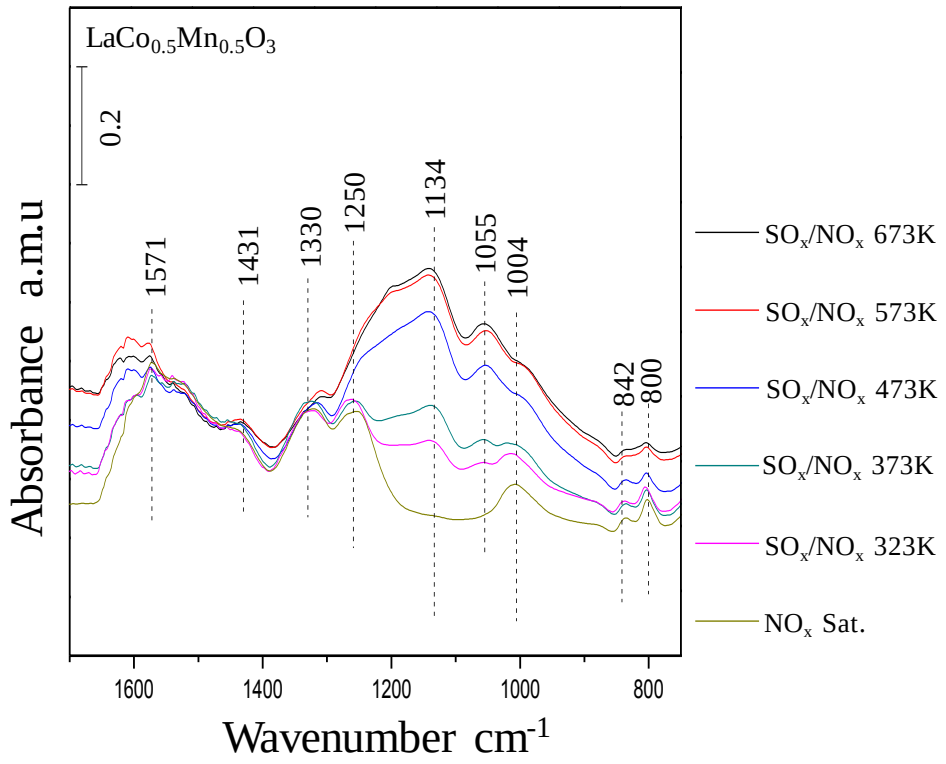

Figure 29.In-situ FTIR spectra for SO_x and NO_x co-adsorption IR on $LaCo_{0.5}Mn_{0.5}O_3$.

sample. In-situ FTIR spectra were acquired for the temperatures in between 373-673 K with 100K increments for 10 min. Figure 28 presents a typical set of in-situ FTIR spectra obtained for the $LaCo_{0.5}Mn_{0.5}O_3$ sample. It can be seen in Figure 28 that SO_x adsorption is rather weak at low temperatures while, NO_x adsorption is almost immediate (e.g. note the NO_x features immediately being generated at 1250, 800, 1004 and 1330 cm^{-1} at 323 K). This indicates that at low temperatures, NO_x species reveal a competitive advantage over SO_x species for binding surface adsorption sites and SO_x adsorption is a rather activated process. This is not surprising as NO_2 adsorption process involves formation of nitrites and nitrates where the oxidative adsorption pathway exploits the atomic oxygen species generated by the self-decomposition of the NO_2 radical. On the other hand, SO_x adsorption process and the formation of sulfite and sulfate species require additional source of oxygen which cannot be provided by the nascent SO_2 molecule but rather implies activation of the molecular oxygen on the surface and O-O bond cleavage. In other words, oxidative SO_x adsorption at low temperatures is hindered due to the kinetic limitations associated with thermal activation and atomic oxygen generation. Figure 29 indicates that with increasing temperature, IR signals at 1134, 1055, and 1571 cm^{-1} due to SO_x species start to intensify in expense of decreasing NO_x vibrational features; suggesting that upon thermal activation strongly bound sulfite and sulfate species start to replace nitrates and nitrites.

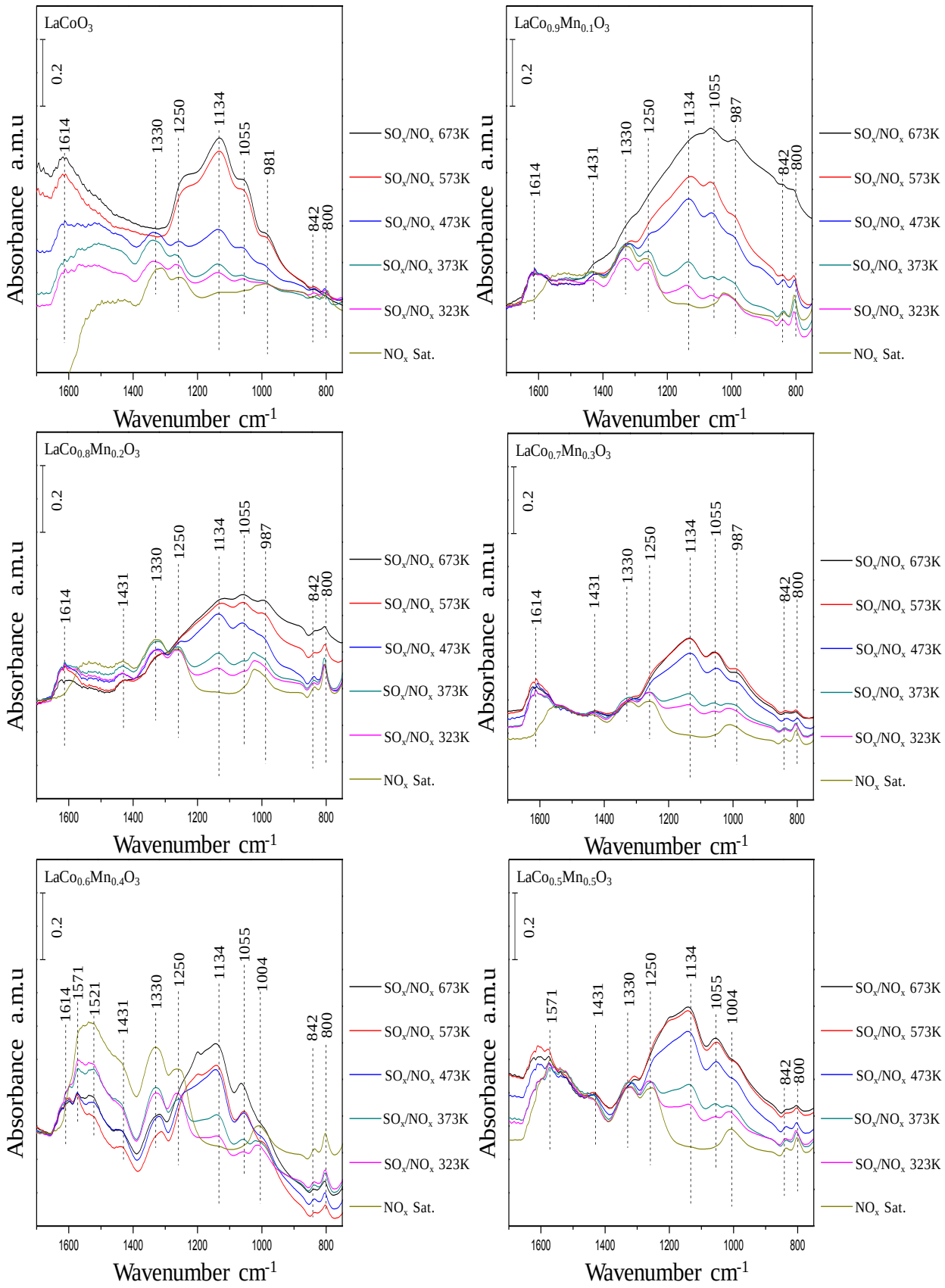

Figure 30. In-situ FTIR SO_x and NO_x co-adsorption IR spectra for $LaCo_xMn_{1-x}O_3$(x=0.0-0.5)

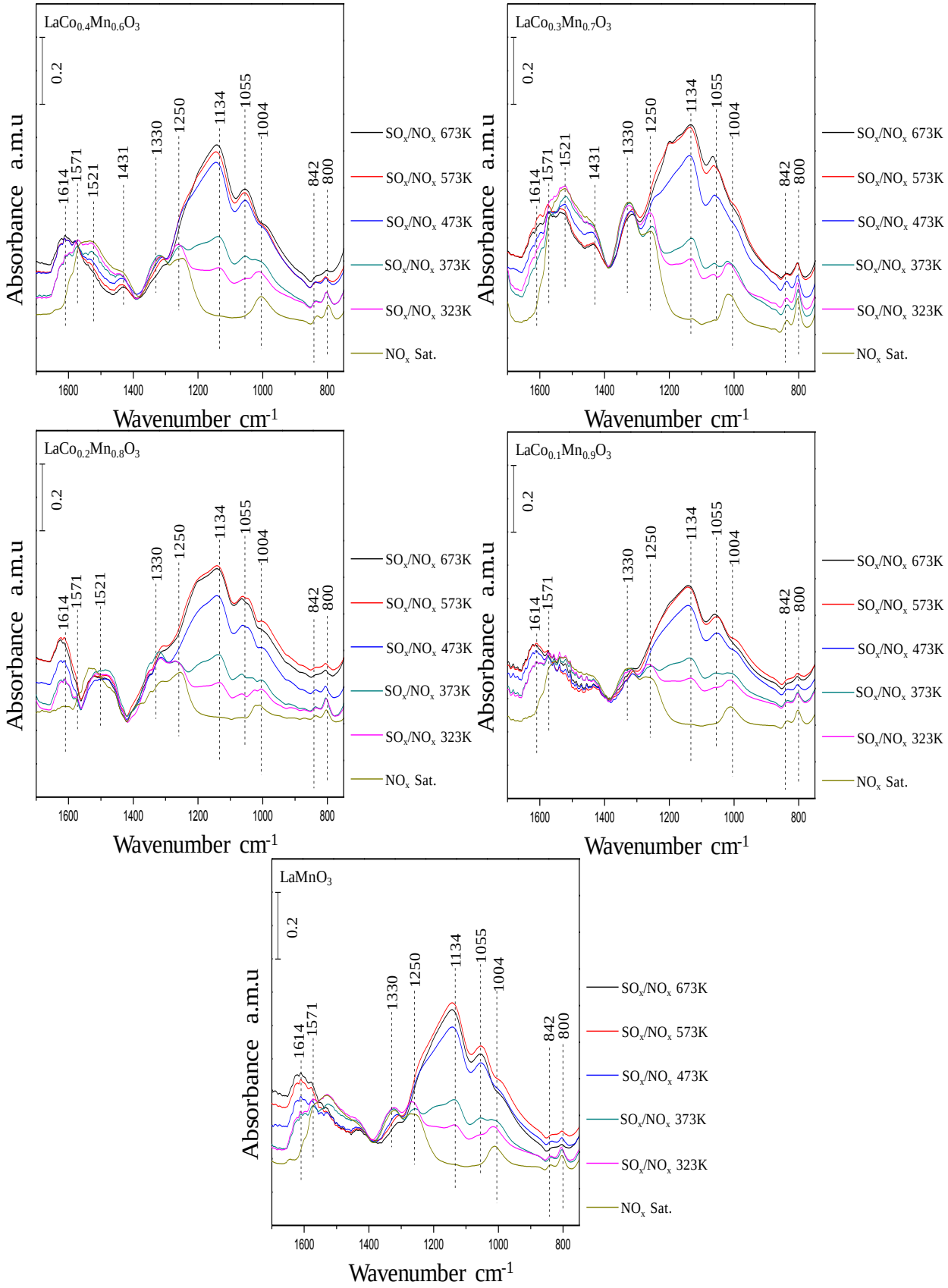

Figure 31. In-sıtu FTIR SO_x and NO_x co-adsorption IR spectra for $LaCo_xMn_{1-x}O_3$ (x=0.6-1.0)

Figures 29 and 30 show similar co-adsorption experiments performed over all of the synthesized hybrid perovskites. A general assessment of these complex set of data suggests that SO_x and NO_x co-adsorption characteristics has a dependence on B-site composition. It is seen that after high temperature (i.e. 673 K) treatment and activation, sulfate species start to dominate perovskite surfaces by replacing most of the nitrates. Nitrate species surviving after this high temperature activation seems to be predominantly monodentate surface nitrates. This is consistent with the fact that due to bidentate sulfite and sulfate species blocking most of the adsorption sites due to their strong adsorption energies, only a limited number of surface sites remain available for NO_x adsorption. Since bidentate nitrates require two empty adjacent surface sites for adsorption, this particular adsorption geometry is rather unfavorable.

3.1.10. O_2 TPD of Perovskites

Oxygen TPD experiments were performed in order to explore the effect of B-site composition on the amount of lattice and surface oxygen present in the structure as well as ease of oxygen desorption, vacancy generation and reduction. Before these experiments, perovskite samples were annealed to 973 K followed by 10 Torr O_2(g) exposure and heating at 773 K for 10 min in oxygen gas. After this oxidation step, samples were cooled in oxygen gas to 323 K and the reactor was evacuated before the TPD data acquisition. During the TPD experiment, m/z=32 desorption channel was recorded in between 323-1173 K using a 12K/min

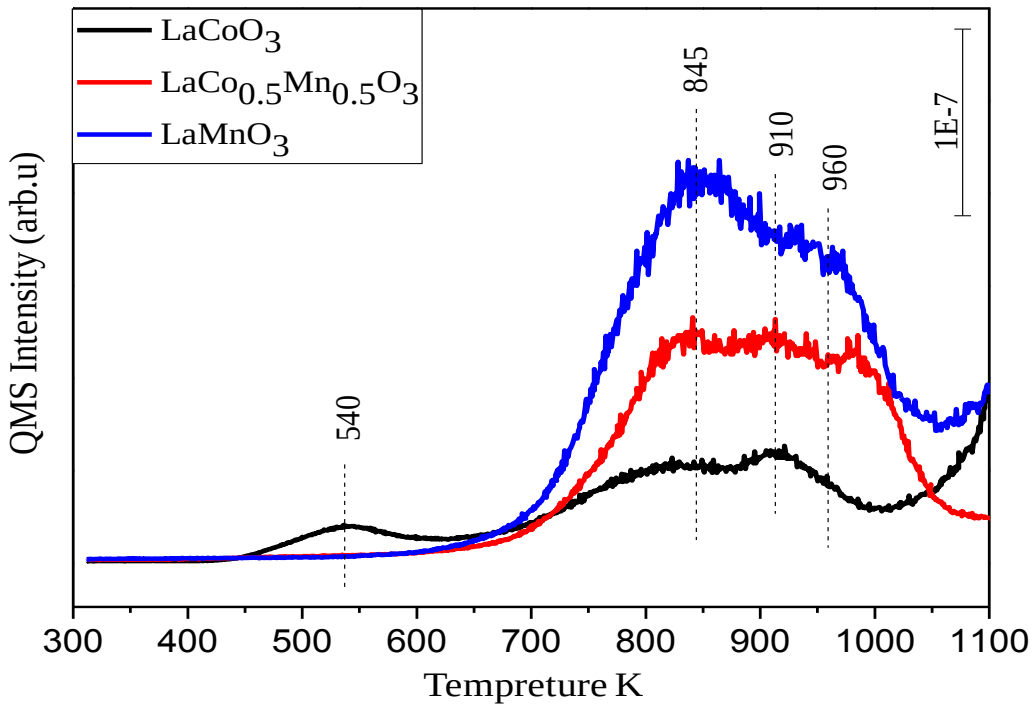

Figure 32. Oxygen TPD profiles for $LaCoO_3$, $LaCo_{0.5}Mn_{0.5}O_3$ and $LaMnO_3$ samples.

linear heating ramp. Desorption signal of oxygen was found to be the most intense for $LaMnO_3$ (Figure 31). This is consistent with the fact that$LaMnO_3$ is an oxygen-rich perovskite due to existence of Mn^{4+} sites in its structure as well as a very high SSA [102], [103]. $LaCoO_3$ yielded the least intense oxygen evolution mostly due to its extremely low surface area. However it is important to note that although Mn-containing perovskites typically release oxygen at high temperatures (i.e. T>800 K), $LaCoO_3$ reveals a uniquely low-temperature oxygen evolution signal at 540K suggesting the presence of extremely readily reducible sites such as Co^{4+} species. Figure 31 and Table 9 indicate that desorbed oxygen amount for $LaCo_{0.5}Mn_{0.5}O_3$ sample is in between two extreme cases (i.e. $LaMnO_3$ and $LaCoO_3$) suggesting that the oxygen evolution and reducibility characteristics of perovskites can be fine-tuned using a specifically designed synthetic protocol.

Table 9. Integrated oxygen desorption signals obtained in O_2-TPD experiments over selected perovskite samples.

Sample Name	**$I_{32}(O_2)$**
$LaMnO_3$	5,59E-5
$LaCo_{0.5}Mn_{0.5}O_3$	3,51E-5
$LaCoO_3$	2,20E-5

3.1.11. H_2 TPR Experiments of Perovskites

H_2 TPR experiments were executed in order to examine the thermal stability of perovskites in a reducing environment under realistic flow-mode conditions. Before the TPR experiments, all samples were treated with %5 H_2/He using a 50 ml/min flow rate. TPR signals were detected via TCD (thermal conductivity detector) and plotted in Figure 32.For Mn-rich perovskites Mn^{4+}→ Mn^{3+} reduction occurs at 553-663 K [102], [103] while the reduction step around 900-1073 K can be assigned toMn^{3+}→ Mn^{2+} [91]. On the other hand for Co-rich

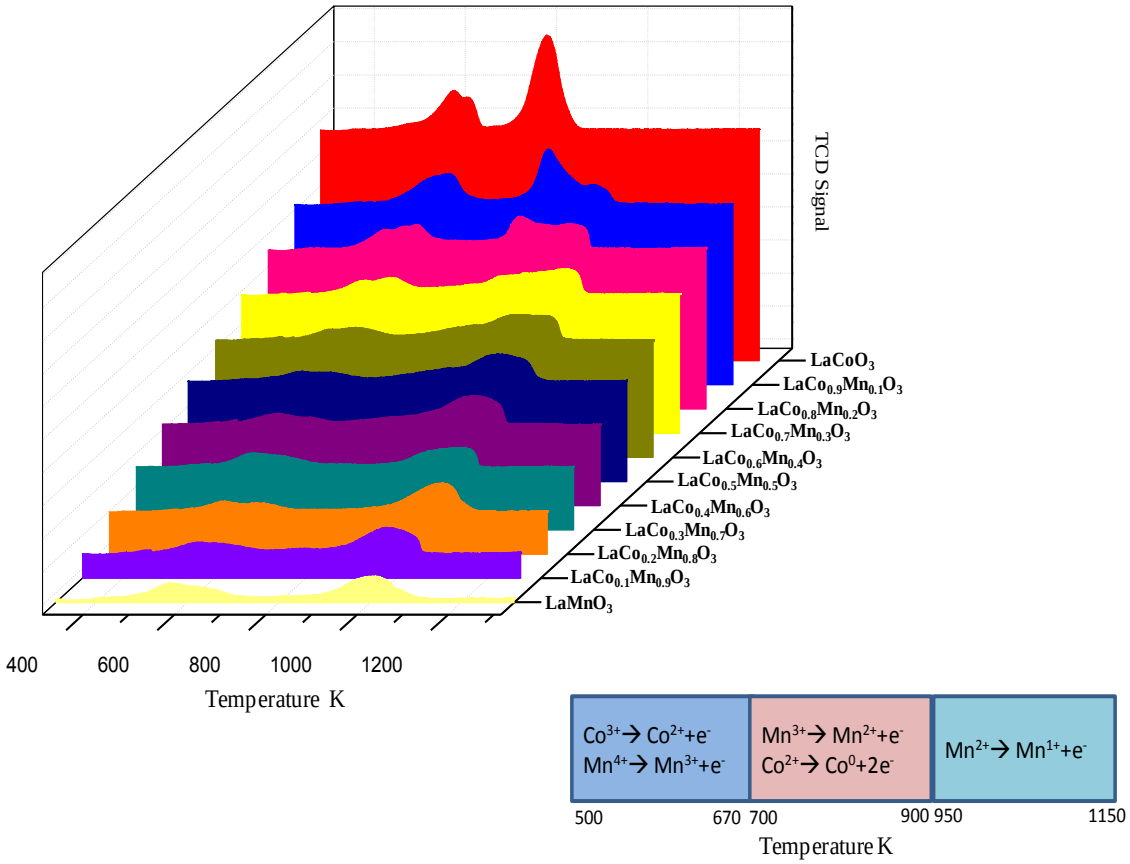

Figure 33.H_2-TPR profiles for $LaCo_xMn_{1-x}O_3$perovskites ($0 \leq x \leq 1.0$) mostly at 673-973 K

materials, reduction process taking place at 553- 643 K can be attributed predominantly to $Co^{3+} \rightarrow Co^{2+}$ with a minor contribution from $Co^{4+} \rightarrow Co^{3+}$. Irreversible reduction of cationic cobalt to metallic cobalt ($Co^{2+} \rightarrow Co^{0}$) occurs [102]. Mn addition to the Co-rich perovskite structure results in a high temperature shift in the $Co^{3+} \rightarrow Co^{2+}$ and $Co^{2+} \rightarrow Co^{0}$ processes suggesting an enhancement of thermal stability under reducing conditions.

Current TPR results are in very good agreement with the previously presented spectroscopic results of the current study pointing to the fact that design and synthesis of hybrid perovskite architectures can be utilized in order to manipulate the surface chemistry, bulk structure, redox character, thermal stability and catalytic properties, in the presence of catalytically relevant oxidizing and reducing agents

Chapter 5

Conclusion

In the current study, simple (i.e. $LaMnO_3$ and $LaCoO_3$) and hybrid perovskites (i.e. $LaCo_xMn_{1-x}O_3$, $0.1 \leq x \leq 0.9$) were synthesized, characterized and their catalytic properties were investigated as a function of B-site composition. Interaction of these perovskite structures with catalytically relevant adsorbates such as NO_2, O_2, H_2 and SO_2 were studied under various oxidizing or reducing conditions via various in-situ and ex-situ spectroscopic techniques. Along these lines, NO_x storage capacities and SO_x poisoning characteristics of such systems were evaluated in a comparative manner. Our main findings can be summarized as follows:

- ✓ Upon calcination at 973 K, $LaMnO_3$ and $LaCo_3$ form cubic and rhombohedral crystal structures; respectively. $LaCo_xMn_{1-x}O_3$ ($0.1 \leq x \leq 0.9$) hybrid perovskites reveal cubic and orthorhombic phases for low and moderate Co loadings while Co-enriched perovskites are comprised of rhombohedral structure.
- ✓ SSA measurements demonstrate that increasing Mn loading in the perovskite structure leads to higher SSA values.
- ✓ Average particles sizes of the synthesized perovskites were determined to within 40-60 nm.

- ✓ XPS results confirm that all of the investigated perovskite surfaces are enriched with La. Surface oxygen amount was found to be the highest for $LaCo_{0.8}Mn_{0.2}O_3$ and $LaCo_{0.7}Mn_{0.3}O_3$ samples.
- ✓ Based on the NO_x TPD results, $LaCo_{0.8}Mn_{0.2}O_3$ and $LaCo_{0.7}Mn_{0.3}O_3$ samples possess the highest NSC.
- ✓ NSC enhancement for $LaCo_{0.8}Mn_{0.2}O_3$ and $LaCo_{0.7}Mn_{0.3}O_3$ samples can be correlated with the unique electronic structure, redox properties of B site cations and the amount of surface oxygen present on the catalysts.
- ✓ N_2 and N_2O formation along during the NO_x TPD experiments suggests that perovskites are capable of N-O bond activation even in the absence of a reducing agent such as H_2.
- ✓ Reduced perovskite surfaces reveal superior NSC compared to their fresh counterparts.
- ✓ Reduction temperature of the B-site cations increase with increasing Mn-content in the hybrid perovskite structure.
- ✓ Amount of oxygen desorption from the hybrid perovskites increases with increasing Mn-content in the hybrid perovskites.
- ✓ SO_x species adsorbed on the perovskites can be reversibly removed from Mn-rich perovskites with the help of a reducing agent such as H_2, while on the Co-rich perovskites, SO_x adsorption yields strongly bound and irreversible bulk-sulfate and sulfite species which cannot be fully removed even in the presence of H_2.

- ✓ Current experimental results demonstrate that perovskites can be fine-tuned in terms their NSC, thermal stability and sulfur tolerance, rendering them promising candidates for NSR systems.

References

[1] "Air Quality Trends," 2015. [Online]. Available: http://www.epa.gov/airtrends/aqtrends.html#airquality.

[2] S. Roy and A. Baiker, "NO x Storage - Reduction Catalysis : From Mechanism and Materials Properties to Storage - Reduction Performance," *Chem. Rev.*, vol. 109, no. 9, pp. 4054–4091, 2008.

[3] W. S. Epling, L. E. Campbell, a Yezerets, N. W. Currier, and J. E. Parks, "Overview of the fundamental reactions and degradation mechanisms of NOx storage/reduction catalysts," *Catal. Rev. Eng.*, vol. 46, no. 2, pp. 163–245, 2004.

[4] R. Burch, "Knowledge and Know-How in Emission Control for Mobile Applications," *Catal. Rev.*, vol. 46, no. 3–4, pp. 271–334, 2004.

[5] V. I. Pârvulescu, P. Grange, and B. Delmon, "Catalytic removal of NO," *Catal. Today*, vol. 46, no. 4, pp. 233–316, 1998.

[6] R. J. Voorhoeve, J. P. Remeika, and D. W. Johnson, "Rare-Earth manganites: catalysts with low ammonia yield in the reduction of nitrogen oxides.," *Science*, vol. 180, no. 4081, pp. 62–64, 1973.

[7] R. J. Voorhoeve, J. P. Remeika, P. E. Freeland, and B. T. Matthias, "Rare-earth oxides of manganese and cobalt rival platinum for the treatment of carbon monoxide in auto exhaust.," *Science*, vol. 177, no. 46, pp. 353–354, 1972.

[8] R. Ramaty, E. T. Byram, T. a Chubb, and H. Friedman, "X-rays from Centaurus A and the Far-Infrared Background Radiation.," *Science*, vol. 171, no. 3970, pp. 500–501, 1971.

[9] P. K. Gallagher, D. W. Johnson, and F. Schrey, "Studies of some supported perovskite oxidation catalysts," *Mater. Res. Bull.*, vol. 9, no. 10, pp. 1345–1352, Oct. 1974.

[10] C. H. Kim, G. Qi, K. Dahlberg, and W. Li, "Strontium-Doped Perovskites Rival," *Science*, vol. 327, no. 5973, pp. 1624–1627, 2010.

[11] M. a Pena and J. L. G. Fierro, "Chemical structures and performances of perovskite oxides," *Chem. Rev.*, vol. 101, no. 7, pp. 1981–2017, 2001.

[12] M. R. Levy, "Chapter 3: Perovskite Perfect Lattice," 2005.

[13] Z. Zhao, X. Yang, and Y. Wu, “Comparative study of Nickel-based perovskite-like mixed oxide catalysts for direct decomposition of NO,” *Appl. Catal. B Environ.*, vol. 8, no. 3, pp. 281–297, 1996.

[14] G. Kremenic, J. M. L. Nieto, J. M. D. Tascon, L. G. Tejuca, T. Nitadori, T. Ichiki, and M. Misono, “Catalytic Properties of Perovskite-Type Mixed Oxides (ABO_3) Consisting of Rare Earth and 3d Transition Metals. The Roles of the A- and B-Site Ions,” *Bull. Chem. Soc. Jpn.*, vol. 61, no. 3, pp. 621–626, 1988.

[15] G. Kremenic, J. M. L. Nieto, J. M. D. Tascon, and L. G. Tejuca, “Chemisorption and catalysis on LaMO3 oxides,” *J. Chem. Soc. Faraday Trans. 1*, vol. 81, no. 4, p. 939, 1985.

[16] M. Futai, C. Yonghua, and Louhui, “Characterization of perovskite-type oxide catalysts RECoO3 by TPR,” *React. Kinet. Catal. Lett.*, vol. 31, no. 1, pp. 47–54, 1986.

[17] M. CRESPIN, “The surface chemistry of some perovskite oxides,” *J. Catal.*, vol. 69, no. 2, pp. 359–370, Jun. 1981.

[18] S. Irusta, M. P. Pina, M. Menéndez, and J. Santamaría, “Catalytic Combustion of Volatile Organic Compounds over La-Based Perovskites,” *J. Catal.*, vol. 179, no. 2, pp. 400–412, Oct. 1998.

[19] S. Royer, F. Bérubé, and S. Kaliaguine, “Effect of the synthesis conditions on the redox and catalytic properties in oxidation reactions of LaCo1-xFexO3,” *Appl. Catal. A Gen.*, vol. 282, no. 1–2, pp. 273–284, 2005.

[20] R. Lago, G. Bini, M. A. Peña, and J. L. G. Fierro, “Partial Oxidation of Methane to Synthesis Gas Using LnCoO3Perovskites as Catalyst Precursors,” *J. Catal.*, vol. 167, no. 1, pp. 198–209, Apr. 1997.

[21] S. Ponce, M. . Peña, and J. L. . Fierro, “Surface properties and catalytic performance in methane combustion of Sr-substituted lanthanum manganites,” *Appl. Catal. B Environ.*, vol. 24, no. 3–4, pp. 193–205, Feb. 2000.

[22] N. Yamazoe, Y. Teraoka, and T. Seiyama, “TPD and XPS study on thermal behavior of absorbed oxygen in La1-XSrXCoO3.,” *Chem. Lett.*, vol. 10, no. 12, pp. 1767–1770, 1981.

[23] S. Kaliaguine, A. Van Neste, V. Szabo, J. E. Gallot, M. Bassir, and R. Muzychuk, “Perovskite-type oxides synthesized by reactive grinding,” *Appl. Catal. A Gen.*, vol. 209, no. 1–2, pp. 345–358, Feb. 2001.

[24] Y. Teraoka, M. Yoshimatsu, N. Yamazoe, and T. Seiyama, “Oxygen-sorptive properties and defect structure of Perovskite-type oxides.,” *Chem. Lett.*, vol. 13, no. 6, pp. 893–896, 1984.

[25] R. Bell, “Influence of synthesis route on the catalytic properties of La1−xSrxMnO3,” *Solid State Ionics*, vol. 131, no. 3–4, pp. 211–220, Jun. 2000.

[26] T. Nakamura, M. Misono, and Y. Yoneda, “Reduction-oxidation and catalytic properties of perovskite-type mixed oxide catalysts (La1-xSrxCoO3).,” *Chem. Lett.*, vol. 10, no. 11, pp. 1589–1592, 1981.

[27] D. Ferri, T. Nakamura, M. Misono, and Y. Yoneda, “Catalytic properties of perovskite-type mixed oxides, La1-xSrxCoO3.,” *Appl. Catal. B Environ.*, vol. 55, no. 2, pp. 119–126, Mar. 1982.

[28] T. Nakamura, M. Misono, and Y. Yoneda, “Catalytic properties of perovskite-type mixed oxides, La1-xSrxCoO3.,” *Bull. Chem. Soc. Jpn.*, vol. 55, no. 2, pp. 394–399, 1982.

[29] T. NITADORI, “Catalytic properties of La1-xA'xMnO3 (A' = Sr, Ce, Hf),” *J. Catal.*, vol. 98, no. 1, pp. 221–228, Mar. 1986.

[30] S. ROYER, D. DUPREZ, and S. KALIAGUINE, “Role of bulk and grain boundary oxygen mobility in the catalytic oxidation activity of LaCo1−xFexO3,” *J. Catal.*, vol. 234, no. 2, pp. 364–375, Sep. 2005.

[31] W. Yang, R. Zhang, B. Chen, N. Bion, D. Duprez, L. Hou, H. Zhang, and S. Royer, “Design of nanocrystalline mixed oxides with improved oxygen mobility: a simple non-aqueous route to nano-LaFeO3 and the consequences on the catalytic oxidation performances.,” *Chem. Commun. (Camb).*, vol. 49, no. 43, pp. 4923–5, 2013.

[32] M. M. Natile, E. Ugel, C. Maccato, and A. Glisenti, “LaCoO3: Effect of synthesis conditions on properties and reactivity,” *Appl. Catal. B Environ.*, vol. 72, no. 3–4, pp. 351–362, Mar. 2007.

[33] P. Jeevanandam, Y. Koltypin, O. Palchik, and A. Gedanken, “Synthesis of morphologically controlled lanthanum carbonate particles using ultrasound irradiation,” *J. Mater. Chem.*, vol. 11, no. 3, pp. 869–873, 2001.

[34] B. Klingenberg and M. A. Vannice, “Influence of Pretreatment on Lanthanum Nitrate, Carbonate, and Oxide Powders,” *Chem. Mater.*, vol. 8, no. 12, pp. 2755–2768, Jan. 1996.

[35] B. M. Gatehouse, S. E. Livingstone, and R. S. Nyholm, “847. Infrared spectra of some nitrato-co-ordination complexes,” *J. Chem. Soc.*, no. 0, pp. 4222–4225, 1957.

[36] J. KUHN and U. OZKAN, “Surface properties of Sr- and Co-doped LaFeO3,” *J. Catal.*, vol. 253, no. 1, pp. 200–211, Jan. 2008.

[37] R. Hammami, H. Batis, and C. Minot, “Combined experimental and theoretical investigation of the CO2 adsorption on LaMnO3+y perovskite oxide,” *Surf. Sci.*, vol. 603, no. 20, pp. 3057–3067, Oct. 2009.

[38] S. Royer, C. Ayrault, C. Carnevillier, F. Epron, P. Marécot, and D. Duprez, “Enthalpy recovery of gases issued from H2 production processes: Activity and stability of oxide and noble metal catalysts in oxidation reaction under highly severe conditions,” *Catal. Today*, vol. 117, no. 4, pp. 543–548, 2006.

[39] P. Mars and D. W. van Krevelen, “Oxidations carried out by means of vanadium oxide catalysts,” *Chem. Eng. Sci.*, vol. 3, pp. 41–59, Jan. 1954.

[40] C. Oliva, M. Allieta, M. Scavini, C. Biffi, I. Rossetti, and L. Forni, “Electron Paramagnetic Resonance Analysis of La1–xMxMnO3+δ (M = Ce, Sr) Perovskite-Like Nanostructured Catalysts,” *Inorg. Chem.*, vol. 51, no. 15, pp. 8433–8440, Aug. 2012.

[41] I. Rossetti, O. Buchneva, C. Biffi, and R. Rizza, “Effect of sulphur poisoning on perovskite catalysts prepared by flame-pyrolysis,” *Appl. Catal. B Environ.*, vol. 89, no. 3–4, pp. 383–390, Jul. 2009.

[42] F. Kapteijn, J. Rodriguez-Mirasol, and J. A. Moulijn, “Heterogeneous catalytic decomposition of nitrous oxide,” Sep. 1996.

[43] D. V Ivanov, L. G. Pinaeva, L. A. Isupova, A. N. Nadeev, I. P. Prosvirin, and L. S. Dovlitova, “Insights into the Reactivity of La1−x Sr x MnO3 (x = 0 ÷ 0.7) in High Temperature N2O Decomposition,” *Catal. Letters*, vol. 141, no. 2, pp. 322–331, 2011.

[44] D. V. Ivanov, E. M. Sadovskaya, L. G. Pinaeva, and L. A. Isupova, “Influence of oxygen mobility on catalytic activity of La–Sr–Mn–O composites in the reaction of high temperature N2O decomposition,” *J. Catal.*, vol. 267, no. 1, pp. 5–13, Oct. 2009.

[45] E. WINTER, “The decomposition of nitrous oxide on the rare-earth sesquioxides and related oxides,” *J. Catal.*, vol. 15, no. 2, pp. 144–152, Oct. 1969.

[46] E. R. S. Winter, “Exchange reactions of oxides. Part IX,” *J. Chem. Soc. A Inorganic, Phys. Theor.* , no. 0, pp. 2889–2902, 1968.

[47] E. WINTER, “The decomposition of nitrous oxide on metallic oxides Part II*1,” *J. Catal.*, vol. 19, no. 1, pp. 32–40, Oct. 1970.

[48] J. P. Dacquin, C. Dujardin, and P. Granger, “Catalytic decomposition of N2O on supported Pd catalysts: Support and thermal ageing effects on the catalytic performances,” *Catal. Today*, vol. 137, no. 2–4, pp. 390–396, Sep. 2008.

[49] J. P. Dacquin, C. Lancelot, C. Dujardin, P. Da Costa, G. Djega-Mariadassou, P. Beaunier, S. Kaliaguine, S. Vaudreuil, S. Royer, and P. Granger, “Influence of preparation methods of LaCoO3 on the catalytic performances in the decomposition of N2O,” *Appl. Catal. B Environ.*, vol. 91, no. 3–4, pp. 596–604, Sep. 2009.

[50] S. Shin, H. Arakawa, Y. Hatakeyama, K. Ogawa, and K. Shimomura, “Absorption of NO in the lattice of an oxygen-deficient perovskite SrFeO3−x and the infrared spectroscopic study of the system NO - SrFeO3−x,” *Mater. Res. Bull.*, vol. 14, no. 5, pp. 633–639, May 1979.

[51] J. Zhu, X. Yang, X. Xu, and K. Wei, “Active Site Structure of NO Decomposition on Perovskite(-like) Oxides: An Investigation from Experiment and Density Functional Theory,” *J. Phys. Chem. C*, vol. 111, no. 3, pp. 1487–1490, Jan. 2007.

[52] J. Zhu, D. Xiao, J. Li, X. Yang, and Y. Wu, “Kinetics and mechanism of NO decomposition over La0.4Sr0.6Mn0.8Ni0.2O3 perovskite-type oxides,” *J. Mol. Catal. A Chem.*, vol. 236, no. 1–2, pp. 182–186, Jul. 2005.

[53] C. Tofan, “Decomposition of nitric oxide over perovskite oxide catalysts: effect of CO2, H2O and CH4,” *Appl. Catal. B Environ.*, vol. 36, no. 4, pp. 311–323, Mar. 2002.

[54] H. Iwakuni, Y. Shinmyou, H. Yano, H. Matsumoto, and T. Ishihara, “Direct decomposition of NO into N2 and O2 on BaMnO3-based perovskite oxides,” *Appl. Catal. B Environ.*, vol. 74, no. 3–4, pp. 299–306, Jul. 2007.

[55] H. Iwakuni, Y. Shinmyou, H. Matsumoto, and T. Ishihara, “Direct Decomposition of NO into N2 and O2 on SrFe0.7Mg0.3O3 Perovskite Oxide,” *Bull. Chem. Soc. Jpn.*, vol. 80, no. 10, pp. 2039–2046, 2007.

[56] C. Tofan, “Direct decomposition of nitric oxide over perovskite-type catalysts Part II. Effect of oxygen in the feed on the activity of three

selected compositions," *Appl. Catal. A Gen.*, vol. 226, no. 1–2, pp. 225–240, Mar. 2002.

[57] T. Ishihara, "Direct decomposition of NO into N2 and O2 over La(Ba)Mn(In)O3 perovskite oxide," *J. Catal.*, vol. 220, no. 1, pp. 104–114, Nov. 2003.

[58] M. Goto, S. Iguchi, K. Katoh, and T. Kihara, "Exhaust gas purification device for an engine," 05-Dec-1995.

[59] K. Kobayashi, T., Yamada, T., and Kayano, "Study of NOx Trap Reaction by Thermodynamic Calculation," *SAE Tech. Pap.*, p. 970745, 1997.

[60] N. Takahashi, H. Shinjoh, T. Iijima, T. Suzuki, K. Yamazaki, K. Yokota, H. Suzuki, N. Miyoshi, S. Matsumoto, T. Tanizawa, T. Tanaka, S. Tateishi, and K. Kasahara, "The new concept 3-way catalyst for automotive lean-burn engine: NOx storage and reduction catalyst," *Catal. Today*, vol. 27, no. 1–2, pp. 63–69, Jan. 1996.

[61] S. Matsumoto, "Catalytic Reduction of Nitrogen Oxides in Automotive Exhaust Containing Excess Oxygen by NOx Storage-Reduction Catalyst," *CATTECH*, vol. 4, no. 2, pp. 102–109, 2000.

[62] S. Takeshima, T. Tanaka, S. Iguchi, Y. Araki, S. Hirota, T. Oda, and F. Murakami, "Exhaust purification device of internal combustion engine," 01-Aug-1995.

[63] Z. LIU and J. ANDERSON, "Influence of reductant on the regeneration of SO-poisoned Pt/Ba/AlO NO storage and reduction catalyst," *J. Catal.*, vol. 228, no. 1, pp. 243–253, Nov. 2004.

[64] S. Elbouazzaoui, E. C. Corbos, X. Courtois, P. Marecot, and D. Duprez, "A study of the deactivation by sulfur and regeneration of a model NSR Pt/Ba/Al2O3 catalyst," *Appl. Catal. B Environ.*, vol. 61, no. 3–4, pp. 236–243, Nov. 2005.

[65] S. Hodjati, K. Vaezzadeh, C. Petit, V. Pitchon, and A. Kiennemann, "Absorption/desorption of NOx process on perovskites: performances to remove NOx from a lean exhaust gas," *Appl. Catal. B Environ.*, vol. 26, no. 1, pp. 5–16, Apr. 2000.

[66] N. Le Phuc, X. Courtois, F. Can, S. Berland, S. Royer, P. Marecot, and D. Duprez, "A study of the ammonia selectivity on Pt/BaO/Al2O3 model catalyst during the NOx storage and reduction process," *Catal. Today*, vol. 176, no. 1, pp. 424–428, Nov. 2011.

[67] N. Le Phuc, X. Courtois, F. Can, S. Royer, P. Marecot, and D. Duprez, “NOx removal efficiency and ammonia selectivity during the NOx storage-reduction process over Pt/BaO(Fe, Mn, Ce)/Al2O3 model catalysts. Part I: Influence of Fe and Mn addition,” *Appl. Catal. B Environ.*, vol. 102, no. 3–4, pp. 353–361, Feb. 2011.

[68] S. Hodjati, C. Petit, V. Pitchon, and A. Kiennemann, “Absorption/desorption of NOx process on perovskites: impact of SO2 on the storage capacity of BaSnO3 and strategy to develop thioresistance,” *Appl. Catal. B Environ.*, vol. 30, no. 3–4, pp. 247–257, Mar. 2001.

[69] J. F. Chen, M. Meng, P. Y. Lin, X. A. Li, Y. L. Fu, and S. M. Yu, “NOx-storage property of BaFeO3 and BaCeO3 perovskite-type oxides,” *CHINESE J. Catal.*, vol. 24, no. 6, pp. 419–422, Jun. 2003.

[70] J. F. Chen, M. Meng, P. Y. Lin, X. G. Li, A. M. Gao, and S. M. Yu, “The NOx storage and resistance of SO2 poison on the BaCeO3 perovskite type oxides,” *CHINESE J. Chem. Phys.*, vol. 16, no. 5, pp. 429–432, Oct. 2003.

[71] H. Xian, X. Zhang, X. Li, L. Li, H. Zou, M. Meng, Q. Li, Y. Tan, and N. Tsubaki, “BaFeO3−x Perovskite: An Efficient NOx Absorber with a High Sulfur Tolerance,” *J. Phys. Chem. C*, vol. 114, no. 27, pp. 11844–11852, Jul. 2010.

[72] H. S. L. M. C. Shin, J. S. Cha, J. H. Lee, S. H. Lee, “Simultaneous Removal of SOx and NOx by Catalytic Cordierite Filter,” *Key Eng. Mater.*, vol. 317–318, pp. 465–468, 2006.

[73] P. Guanghong, M. Ming, and L. Xingang, “Preparation, Structure and Performance of Defected Perovskite BaCo1-xFexO3-delta Catalyst for NOx Storage and Reduction,” *CHINESE J. Catal.*, vol. 32, no. 1, pp. 135–138, Jan. 2011.

[74] Z. Li, M. Meng, Q. Li, Y. Xie, T. Hu, and J. Zhang, “Fe-substituted nanometric La0.9K0.1Co1−xFexO3−δ perovskite catalysts used for soot combustion, NOx storage and simultaneous catalytic removal of soot and NOx,” *Chem. Eng. J.*, vol. 164, no. 1, pp. 98–105, Oct. 2010.

[75] H. Xian, F.-L. Li, X.-G. Li, X.-W. Zhang, M. Meng, T.-Y. Zhang, and N. Tsubaki, “Influence of preparation conditions to structure property, NOx and SO2 sorption behavior of the BaFeO3−x perovskite catalyst,” *Fuel Process. Technol.*, vol. 92, no. 9, pp. 1718–1724, Sep. 2011.

[76] C. H. Kim, W. Li, and K. A. Dahlberg, “Method and architecture for oxidizing nitric oxide in exhaust gas from hydrocarbon fuel source with a fuel lean combustion mixture.” Google Patents, 2011.

[77] J. DEBOER, “Studies on pore systems in catalysts VII. Description of the pore dimensions of carbon blacks by the t method,” *J. Catal.*, vol. 4, no. 6, pp. 649–653, Dec. 1965.

[78] E. Kayhan, “Structure and NOx uptake properties of Fe-Ba/Al2O3 as a model NOx storage material,” Bilkent University, 2009.

[79] I. Twagirashema, M. Frere, L. Gengembre, C. Dujardin, and P. Granger, “Structural regeneration of LaCoO3 perovskite-based catalysts during the NO + H2 + O2 reactions,” *Top. Catal.*, vol. 42–43, no. 1–4, pp. 171–176, 2007.

[80] Z. Say, M. Dogac, E. I. Vovk, Y. E. Kalay, C. H. Kim, W. Li, and E. Ozensoy, “Palladium doped perovskite-based NO oxidation catalysts: The role of Pd and B-sites for NOx adsorption behavior via in-situ spectroscopy,” *Appl. Catal. B Environ.*, vol. 154–155, pp. 51–61, Jul. 2014.

[81] Y. Wu, C. Cordier, E. Berrier, N. Nuns, C. Dujardin, and P. Granger, “Surface reconstructions of LaCo1−xFexO3 at high temperature during N2O decomposition in realistic exhaust gas composition: Impact on the catalytic properties,” *Appl. Catal. B Environ.*, vol. 140–141, pp. 151–163, Aug. 2013.

[82] G. Pecchi, C. Campos, and O. Peña, “Thermal stability against reduction of LaMn1-yCoyO3 perovskites,” *Mater. Res. Bull.*, vol. 44, no. 4, pp. 846–853, 2009.

[83] P. Scherrer, “Bestimmung der Größe und der inneren Struktur von Kolloidteilchen mittels Röntgenstrahlen,” *Nachrichten von der Gesellschaft der Wissenschaften zu Göttingen, Math. Klasse*, vol. 1918, pp. 98–100.

[84] “Voigt Function,” 2015. [Online]. Available: http://www.originlab.com/doc/Origin-Help/Voigt-FitFunc.

[85] Z. Chen, C. H. Kim, L. T. Thompson, and W. F. Schneider, “LDA+U evaluation of the stability of low-index facets of LaCoO3 perovskite,” *Surf. Sci.*, vol. 619, pp. 71–76, Jan. 2014.

[86] S. O. Choi, M. Penninger, C. H. Kim, W. F. Schneider, and L. T. Thompson, “Experimental and Computational Investigation of Effect of Sr on NO Oxidation and Oxygen Exchange for La 1– x Sr x CoO 3 Perovskite Catalysts,” *ACS Catal.*, vol. 3, no. 12, pp. 2719–2728, 2013.

[87] M. W. Penninger, C. H. Kim, L. T. Thompson, and W. F. Schneider, “DFT Analysis of NO Oxidation Intermediates on Undoped and Doped LaCoO3 Perovskite,” *J. Phys. Chem. C*, vol. 119, no. 35, pp. 20488–20494, Sep. 2015.

[88] N. MERINO, B. BARBERO, P. GRANGE, and L. CADUS, “LaCaCoO perovskite-type oxides: preparation, characterisation, stability, and catalytic potentiality for the total oxidation of propane,” *J. Catal.*, vol. 231, no. 1, pp. 232–244, Apr. 2005.

[89] H. Wang, Z. Zhao, P. Liang, C. Xu, A. Duan, G. Jiang, J. Xu, and J. Liu, “Highly Active La1−x K x CoO3 Perovskite-type Complex Oxide Catalysts for the Simultaneous Removal of Diesel Soot and Nitrogen Oxides Under Loose Contact Conditions,” *Catal. Letters*, vol. 124, no. 1–2, pp. 91–99, 2008.

[90] C. Bernard, B. Durand, M. Verelst, and P. Lecante, “Hydrothermal synthesis of LaMnO3+δ: F.T.I.R. and W.A.X.S. investigations of the evolution from amorphous to crystallized powder,” *J. Mater. Sci.*, vol. 39, no. 8, pp. 2821–2826, 2004.

[91] F. E. López-Suárez, M. J. Illán-Gómez, A. Bueno-López, and J. A. Anderson, “NOx storage and reduction on a SrTiCuO3 perovskite catalyst studied by operando DRIFTS,” *Appl. Catal. B Environ.*, vol. 104, no. 3–4, pp. 261–267, May 2011.

[92] B. Klingenberg and M. A. Vannice, “NO adsorption and decomposition on La2O3 studied by DRIFTS,” *Appl. Catal. B Environ.*, vol. 21, no. 1, pp. 19–33, May 1999.

[93] A. Martinez-Arias, J. Soria, J. C. Conesa, X. L. Seoane, A. Arcoya, and R. Cataluna, “NO reaction at surface oxygen vacancies generated in cerium oxide,” *J. Chem. Soc. Faraday Trans.*, vol. 91, no. 11, pp. 1679–1687, 1995.

[94] K. I. HADJIIVANOV, “Identification of Neutral and Charged N x O y Surface Species by IR Spectroscopy,” *Catal. Rev.*, vol. 42, no. 1–2, pp. 71–144, May 2000.

[95] F. Prinetto, G. Ghiotti, I. Nova, L. Lietti, E. Tronconi, and P. Forzatti, “FT-IR and TPD Investigation of the NOx Storage Properties of BaO/Al2O3 and Pt−BaO/Al2O3 Catalysts,” *J. Phys. Chem. B*, vol. 105, no. 51, pp. 12732–12745, Dec. 2001.

[96] G. Ghiotti and A. Chiorino, “An IR study of NO adsorption on a CrOx/ZrO2 catalyst,” *Spectrochim. Acta Part A Mol. Spectrosc.*, vol. 49, no. 9, pp. 1345–1359, Aug. 1993.

[97] “NIST Chemistry WebBook,” *NIST Standard Reference Database Number 69.* .

[98] E. Emmez, E. I. Vovk, V. I. Bukhtiyarov, and E. Ozensoy, “Direct Evidence for the Instability and Deactivation of Mixed-Oxide Systems: Influence of Surface Segregation and Subsurface Diffusion,” *J. Phys. Chem. C*, vol. 115, no. 45, pp. 22438–22443, Nov. 2011.

[99] M. Waqif, P. Bazin, O. Saur, J. C. Lavalley, G. Blanchard, and O. Touret, “Study of ceria sulfation,” *Appl. Catal. B Environ.*, vol. 11, no. 2, pp. 193–205, Feb. 1997.

[100] I. Rosso, S. Fiorilli, B. Onida, G. Saracco, and E. Garrone, “Sulfate Species in MgO-Supported LaMn0.5Mg0.5O3 Perovskites: An Insight into the Chemistry of MgO,” *J. Phys. Chem. B*, vol. 106, no. 46, pp. 11980–11984, Nov. 2002.

[101] M. Bensitel, M. Waqif, O. Saur, and J. C. Lavalley, “The structure of sulfate species on magnesium oxide,” *J. Phys. Chem.*, vol. 93, no. 18, pp. 6581–6582, Sep. 1989.

[102] R. Lago, G. Bini, M. a Pe, and J. L. G. Fierro, “Partial Oxidation of Methane to Synthesis Gas Using LnCoO 3 Perovskites as Catalyst Precursors,” vol. 209, pp. 198–209, 1997.

[103] Y. N. Lee, R. M. Lago, J. L. G. Fierro, V. Cortés, F. Sapiña, and E. Martínez, “Surface properties and catalytic performance for ethane combustion of La1-xKxMnO3+δ perovskites,” *Appl. Catal. A Gen.*, vol. 207, no. 1–2, pp. 17–24, 2001.